Thesis for the degree
Master of Science

Submitted to the Scientific Council of the
Weizmann Institute of Science
Rehovot, Israel

עבודת גמר (תזה) לתואר
מוסמך למדעים

מוגשת למועצה המדעית של
מכון ויצמן למדע
רחובות, ישראל

By
Aviram Uri

מאת
אבירם אורי

ייצור ואפיון של התקן התאבכות קוונטית מוליך-על רב ערוצי על חוד.

Fabrication and characterization of multi-junction, multi-terminal superconducting quantum interference device on a tip.

Advisor:
Prof. Eli Zeldov

מנחה:
פרופ' אלי זלדוב

February 2014

שבט התשע"ה

Acknowledgments

This work would not have been possible without the help of my co students in the Eli Zeldov lab. I am in debt to them for the endless support, good advice, ideas, encouragement and many productive conversations over coffee. I thank Lior Embon for his design of the tip holder and for his patience in explaining various physics and software related issues. Dr. Yonathan Anahory for sharing his experimental knowledge and experience, for the algorithm of finding the low noise working points and for the development of Pb SOTs. Dr. Andrea Young for his idea to measure noise using a diode (and for insisting that it will eventually work) and for the home made DAC & ADC boxes. These took the quality of the measurements up a notch. Ella Orion Lachman for making the DAC & ADC boxes work in very short time and for her help in solving various problems on a daily basis. Dorri Halbertal for his heat transfer calculation that helped solve the adhesion problem. Dr. Naren Hoovinakatte for the high pressure exchange gas idea which ultimately solved the adhesion problem. Dr. Jo Cuppens for the good advice and spirits. Dr. Yuri Myasoedov for his high skills and craftsmanship required for the fabrication of the MSOT contacts. Dr. Alexander Meltzer for the theoretical analysis that allowed us to understand the basic mechanism underlying the MSOT. Anton Yakovenko for his help with the simulation. Dr. Michael Rappaport for his help and experience. Prof. Martin E. Huber for all the electronics, the good advice and the patience.

I thank my advisor Prof. Eli Zeldov for always being available for discussion and for seeing very clearly what is the right solution to every problem we encountered. His sharp mind and strong physical intuition were essential to the project's success. It was a pleasure to work under his guidance and I thank you for the opportunity.

Lastly, I thank my wife Gal for her support, my young daughter Erel for her good spirits and smile and my family for my physics education that began at a young age.

This work is dedicated to the memory of my mother Yael whom we love and miss with all our hearts.

Abstract

A novel Multi-junction, multi-terminal SQUID-On-Tip (MSOT) was fabricated by Pb deposition on the apex of a sharp pulled quartz pipette with a unique cross section. The MSOT has 4 terminals and 4 weak links, compared with the 2 terminals and 2 weak links of a conventional SQUID. These extra degrees of freedom allow in-situ control of the critical current dependency on applied magnetic flux $I_c(\Phi_a)$, eliminating low response regions, or 'blind spots', that are intrinsic to SQUID devices and appear at integer flux quanta. A continuous operation of the SQUID at its highest sensitivity over the entire field range up to H_{c2} is achieved without the use of pickup or feedback loops. The MSOT presented in this work has a diameter of 165 nm and a magnetic flux noise of $\sqrt{S_\Phi} < 370\ \mathrm{n}\Phi_0/\sqrt{\mathrm{Hz}}$ which corresponds to a spin noise of $\sqrt{S_n} < 11\ \mu_B/\sqrt{\mathrm{Hz}}$ and magnetic field noise of $\sqrt{S_B} < 34\ \mathrm{nT}/\sqrt{\mathrm{Hz}}$ at 30 ± 5 kHz for a *continuous* magnetic field range from 0 to 0.75 T. In the majority of this field range, the noise levels are as low as $200\ \mathrm{n}\Phi_0/\sqrt{\mathrm{Hz}}$, $6\ \mu_B/\sqrt{\mathrm{Hz}}$ and $20\ \mathrm{nT}/\sqrt{\mathrm{Hz}}$. In the future the MSOT will be incorporated into the existing scanning system in our laboratory, expanding its imaging capabilities.

Contents

List of abbreviations

SQUID - Superconducting QUantum Interference Device

SOT - SQUID-On-Tip

MSOT - Multi-junction, multi-terminal SOT

SC - SuperConducting

SEM - Scanning Electron Microscope

SSAA - Series SQUID Array Amplifier

DAC - Digital to Analog Converter

ADC - Analog to Digital Converter

WP - Working Point

CPR - Current-Phase Relation

GL - Ginzburg Landau

1 Introduction

This introduction gives a short description of the currently available tools for magnetic imaging and the advantages the MSOT brings with it. The reader is assumed to have basic knowledge of Superconducting QUantum Interference Devices (SQUIDs) . For a broader, more basic background on the field, see section 2.

1.1 Magnetic field imaging

Local magnetic field imaging at the nanoscale is one of the key elements in understanding a variety of fundamental physics. This includes topological insulators, spin Hall effect, quantum spin Hall effect, fractional quantum Hall effect, unconventional superconductors and Majorana fermions. It can also contribute significantly to discovering new fundamental physical phenomena. Since the magnetic field of a nanostructure decays rapidly with distance r, as r^{-3}, the sensitivity will ultimately be limited by the separation between the sample and the probe [1] and in order to achieve nanoscale resolution one has to approach and scan the sample at a few nm above the surface. A milestone in nanoscale imaging is the ability to measure the magnetic signal of a single electron, one Bohr magnetron μ_B [1, 2].

Figure 1 adapted from [3] compares the currently available magnetic imaging tools in terms of their magnetic field and magnetic moment sensitivities. The r^{-3} dependency of the magnetic signal on the dipole-probe separation r is expressed by the $-1/3$ slope of the equi-spin-sensitivity lines in this log-log map. Both magnetic resonance force microscopy (MRFM) [4] and diamond nitrogen vacancy (NV) sensors [2, 5, 6, 7] show relatively high spin sensitivity. Each of them, however, has its limitations and is suitable for specific situations. MRFM is invasive which is limiting in many cases, whereas NV sensors are difficult to operate at cryogenic temperatures which is the regime of most quantum physics phenomena. Micro-Hall sensors [8] and conventional SQUIDs [9, 10] are based on planar fabrication methods and as such, they typically cannot be brought to the surface of the sample and scanned within a distance of less than few hundred nm.

The SQUID is sensitive to the magnetic flux Φ penetrating its loop. Typical SQUIDs have flux noise of order $\sqrt{S_\Phi} \lesssim 1\ \mu\Phi_0/\sqrt{\text{Hz}}$. The magnetic field noise is related to the flux noise by $\sqrt{S_B} = \sqrt{S_\Phi}/A$, where A is the SQUID's loop area, so that large SQUIDs are suitable for measuring magnetic fields that are constant over space (assuming the flux noise does not depend on the SQUID's loop size). Measuring magnetic fields at the nanoscale, however, brings the need for small SQUIDs since the spatial resolution is limited by roughly the loop diameter D. For a normal oriented dipole at the centerline of a SQUID of radius R, the spin noise $\sqrt{S_n}$ in units of $\mu_B/\sqrt{Hz}$ is [9, 11]:

$$\sqrt{S_n} = \sqrt{S_\Phi}\frac{R}{r_e}\left(1+\frac{z^2}{R^2}\right)^{3/2},$$

where z is the height of the SQUID above the dipole, $r_e \approx 2.82 \times 10^{-15}$ m is the classical radius

of the electron and the flux noise $\sqrt{S_\Phi}$ is given in units of $\Phi_0/\sqrt{\text{Hz}}$, $\Phi_0 = \frac{h}{2e} = 20.7\ G \times \mu\text{m}^2 = 2.07 \times 10^{-15}$ Wb being the flux quantum, h is Plank's constant and e the electron charge. This shows that the closer the SQUID is to the dipole, the lower the spin noise. When the SQUID is far away from the dipole ($z \gg R$) then $\sqrt{S_n} \approx \sqrt{S_\Phi}\frac{z^3}{r_e R^2}$, so that the spin noise is smaller for larger diameter SQUIDs. However, in the other limit, of $z \ll R$ we have

$$\sqrt{S_n} \approx \sqrt{S_\Phi}\frac{R}{r_e} \quad (z \ll R)\,, \tag{1}$$

thus high sensitivity to magnetic dipoles requires a probe as small as possible scanning as close as possible to the sample. The spin noise presented in this work is calculated according to equation 1, assuming the spin is in the center of the SQUID loop. We note that in the intermediate case, when $z = R$, the spin noise is ~3 times higher than in the $z = 0$ case.

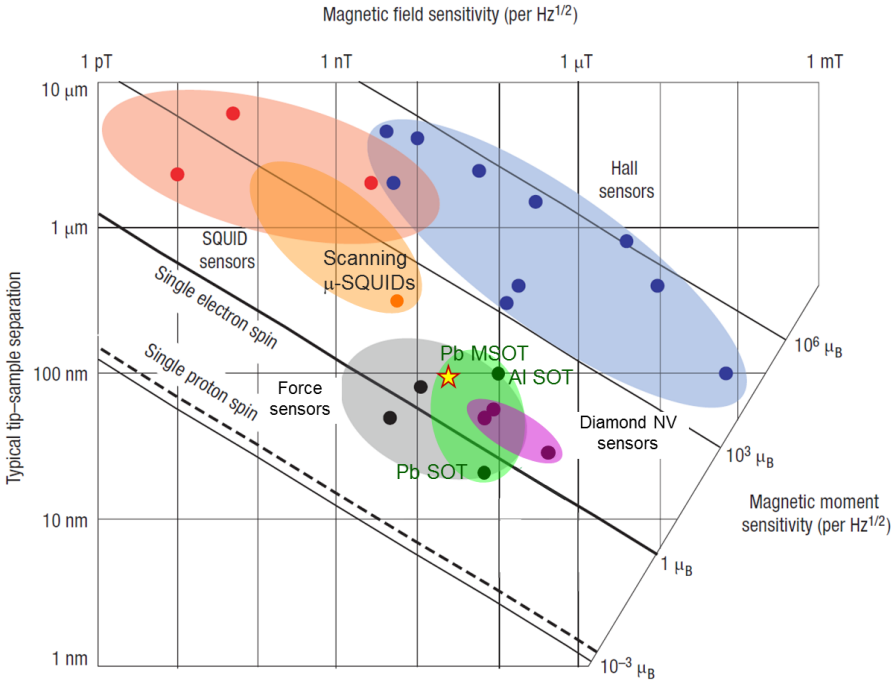

Figure 1: Comparison of different magnetic imaging sensors, adapted from [3]. The SQUIDs made in our lab are shown in green and the device presented in this work is marked by a star.

1.2 The SQUID-On-Tip (SOT)

Over the last few years we have developed in our group a SQUID fabrication technique that does not involve lithography. Our SQUIDs [1, 12, 13, 14, 15] are fabricated on the apex of a very sharp quartz pipette which also gives them their name: SQUID-On-Tip. This is the ideal geometry for scanning probe microscopy as is sets almost no limitation on the sample-probe distance. Effective diameters down to 46 nm [1] are achieved, which is approximately an order of magnitude smaller than the limit set by lithographically fabricated SQUIDs and a record spin sensitivity of 0.38 $\mu_B/\sqrt{\text{Hz}}$ was reported

[1].

A hollow quartz tube with an outer diameter of 1 mm and an inner diameter of 0.5 mm is pulled into a sharp pipette using Sutter Instruments P-2000 micro-pipette puller. An evaporator is used to deposit superconducting (SC) thin films in three self-aligned steps to create a SQUID, as illustrated in Figure 2. Firstly, a thin film is deposited on one side of the pipette forming an electrode. Then the tip is rotated in-situ and a second electrode is deposited on its other side. Lastly, the tip is rotated so that it points toward the source and the ring is deposited. The result is a SQUID loop that is interrupted by two Dayem bridge weak links that are formed at the regions that are closest to the gaps between the electrodes. The effective diameter of the loop can be set to values ranging from 1 μm to 50 nm by changing the pulling parameters. We currently have a high yield, highly reproducible fabrication procedure for Al [12, 13, 14] and Pb [1] SOTs. The SOT is integrated into a scanning microscope to produce images with very high spatial resolution and magnetic field sensitivity [16].

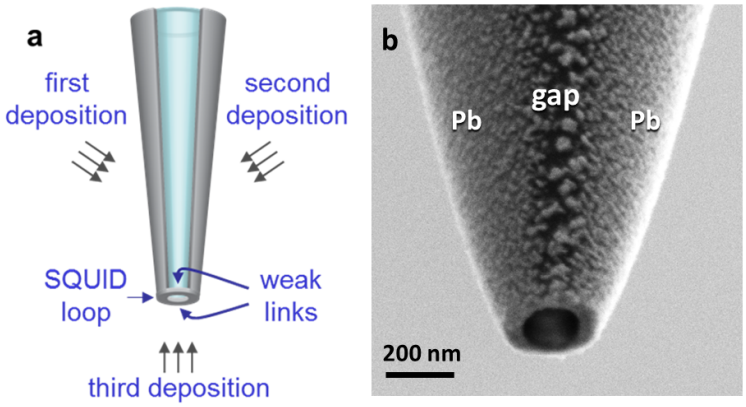

Figure 2: (**a**) Illustration of the SOT fabrication method using three self-aligned deposition steps resulting in two leads along the sides of a pulled quartz pipette separated by a gap and a SQUID loop with two weak links formed at the apex. The thickness of the superconducting films is typically 25 nm for the leads and 15 nm for the ring. (**b**) Scanning electron microscope (SEM) image of a Pb SOT with an effective diameter of 162 nm.

The SQUID's maximal dissipationless current I_c is modulated with the magnetic flux Φ penetrating its loop $I_c = I_c(\Phi)$, which makes the SQUID a magnetometer. The dependency of the critical current on the flux is $I_c \sim |\cos(\pi\Phi/\Phi_0)|$ [17] which has a period of one flux quantum Φ_0. The response $dI_c/d\Phi$ is also periodic with the same period and goes to zero at integer flux quanta, making it impossible to sense small changes in magnetic flux around these so called 'blind spots'.

To overcome this problem conventional SQUID magnetometers work in a flux locked loop (FLL) setup. The FLL is implemented by a pickup coil, which couples the magnetic signal of the sample to a remote SQUID and a feedback coil that maintains constant flux through the SQUID keeping it at its most sensitive operation point. The geometry of the SOTs, and the close proximity to the sample, however, limits the ability to incorporate these two coils and use the SOT in a FLL operation mode, which is a significant shortcoming of the SOT. The problem is even more acute for our small diameter

SOTs, with periods of up to 1 T, where the blind spots span over a wide range of fields [1], usually centered around zero field.

1.3 The Multi-SOT (MSOT)

To address the limitation described above we hereby present a radically new device – a Multi-terminal multi-junction SOT (MSOT) with unique in-situ electronic control and tuneability. A schematic and SEM images of the MSOT are given in Figure 3. A quartz tube of 1 mm outer diameter and 0.4 mm inner diameter with four grooves is used as a substrate. The pulled tube is deposited with SC thin films, similarly to the SOT. The result is a SQUID with four leads, four gaps along the grooves between the leads and four weak links on the ring near the gapped regions.

Operating the MSOT with terminals 1 and 3 only, keeping terminals 2 and 4 floating results in a right-left symmetric SQUID, where each side of the loop is interrupted with two weak links (instead of one in the case of conventional SQUIDs). In this setup the dependency $I_c(\Phi)$ is very similar to that of conventional SQUIDs. However, driving current through terminal 2 (or 4) enables in-situ shifting of the $I_c(\Phi)$ curve along the Φ axis and brings the most sensitive points to the desired flux value. A continuous operation of the SQUID over the entire field range up to H_{c2} is readily achieved without pickup or feedback loops and enables operation at highest sensitivity for any applied field, eliminating the blind spots. The MSOT has all the strong points of the SOT and also gives an alternative to replacing the FLL operation mode allowing high sensitivity throughout its dynamic field range.

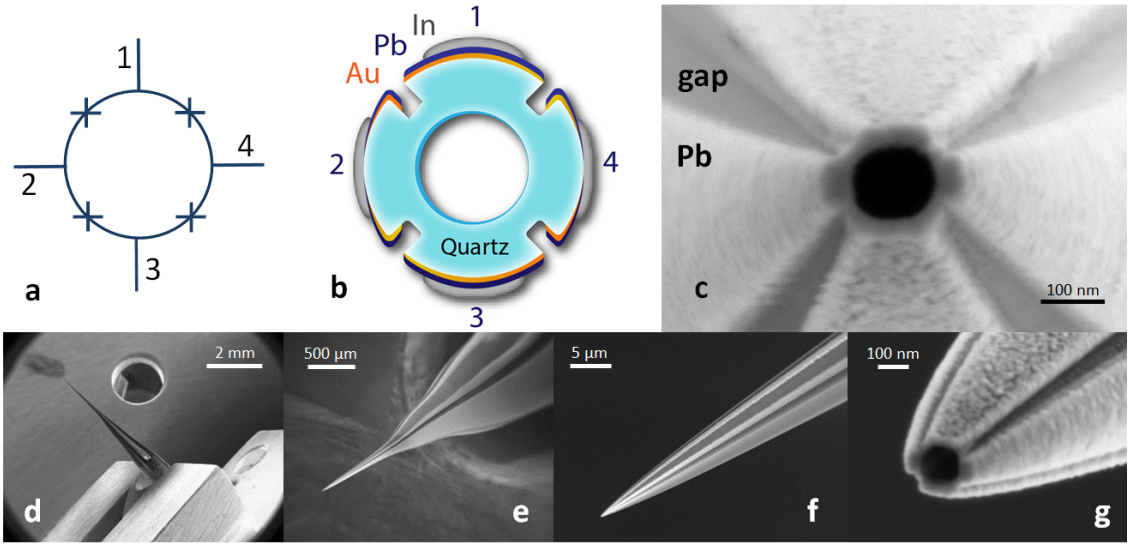

Figure 3: MSOT fabrication: (**a**) MSOT schematics, showing the four terminals and four Dayem bridges. (**b**) Deposition schematics, showing a cross section of the 1 mm diameter quartz tube with the four grooves, the deposited Au contacts, the deposited SC Pb thin film and the In applied by soldering iron. (**c**)-(**g**) SEM images of the Pb MSOT presented in this work that has an effective diameter of 165 nm, showing the four Pb electrodes, the four gaps between them and the four Dayem bridges that are formed on the ring at the regions closest to the gaps.

2 Basic theory of SQUIDs

This section gives the theory that forms the basis for the SQUID's operation. Readers that are familiar with the basic theory can skip directly to section 3. However, there are a few more advanced topics addressed in this section that are sometimes ignored in less specialized texts. These include small SQUIDs with Dayem bridges which is the case for the SOT and the MSOT.

2.1 Superconductivity

Superconductivity is a quantum phase of matter where Cooper pairing [18] of electrons results in a macroscopic behavior characterized by both dissipationless current flow [19] and perfect diamagnetism, known as the Meissner effect [20]. The microscopic theory of superconductivity is the BCS theory by Bardeen, Cooper and Schrieffer [21]. It shows that the weak attractive phonon mediated interaction between electrons is enough to create bound pairs of electrons with equal and opposite spin, called Cooper pairs, that are the charge carriers in the superconducting state. Below a critical temperature T_c all the pairs in the condensate are highly correlated in momentum space. Roughly speaking, this means all the pairs move with the same center of mass velocity which accounts for the dissipationless flow. BCS theory suggests that the bound pair is favorable in energy over two unbound electrons, or quasiparticles. This energy difference per electrons is denoted Δ and it is temperature dependent. As the temperature is raised from $T = 0$ the energy gap decreases until it reaches $\Delta = 0$ at T_c. Above T_c electron pairing is no longer favorable and a second order phase transition occurs.

At temperatures around T_c the Ginzburg-Landau (GL) theory [22] is applicable. It is a macroscopic phenomenological theory, as part of Landau's general theory for second order phase transitions that focuses on the condensate rather than on the excitations. The GL theory can be derived from the BCS theory for the special case of $T \approx T_c$ [23] and includes a very important generalization to spatial dependency not available in the BCS framework. While the BCS theory can be used to calculate the values of the parameters used in the phenomenological theory, the GL theory is a practical tool for understanding a wide variety of superconductivity related phenomena. Practically, in many cases the restriction $T \approx T_c$ is pushed to the limit as the GL theory is used to describe phenomena well below T_c. In cases like this an experimental justification is usually in place. The theory defines a complex order parameter $\psi(\mathbf{r},t)$ that describes a macroscopic pseudo wave function which is of key importance:

$$\psi(\mathbf{r},t) = \psi_0(\mathbf{r},t)\, e^{i\varphi(\mathbf{r},t)}.$$

The amplitude of the pseudo wave function describes the density of electron pairs n_s:

$$|\psi(\mathbf{r},t)|^2 = n_s(\mathbf{r},t),$$

and the phase $\varphi(\mathbf{r},t)$ describes their center of mass motion. The pseudo wave function obeys the GL

equation [17]

$$\alpha\psi+\beta\left|\psi\right|^{2}\psi+\frac{1}{2m^{*}}\left(\frac{\hbar}{i}\nabla-\frac{e^{*}}{c}\mathbf{A}\right)^{2}\psi=0,$$

where e^{*} and m^{*} are the effective charge and mass of the charge carriers respectively and $\mathbf{A}$ denotes the vector potential. At least for traditional (BCS) superconductors the cooper pairing means $e^{*}=2e$ and $m^{*}=2m_{e}$ (if we ignore dressed electron effects). The wave function thus obeys a Schrödinger-like equation, including a nonlinear term $\sim\left|\psi(\mathbf{r},t)\right|^{2}$. This term means it is energetically favorable for the condensate to be spread evenly in space (very similar to the energies of the electric and magnetic fields, which go as E^{2} and B^{2} respectively and describes favoring of even spreading of the fields in space). Since all the pairs around a macroscopic region in space share the same center of mass velocity $\mathbf{v}_{s}$, the phase is well defined over macroscopic distances. The gauge invariant probability current is related to the pseudo wave function by

$$\mathbf{J}_{\rho}=\frac{\left|\psi\right|^{2}}{m^{*}}\left(\hbar\nabla\varphi-\frac{e^{*}}{c}\mathbf{A}\right)=\left|\psi\right|^{2}\mathbf{v}_{s},$$

and the electrical current density is simply

$$\mathbf{J}=n_{s}e^{*}\mathbf{v}_{s}.$$

2.2 Fluxoid quantization

Another important consequence of the well defined wave function is the Fluxoid quantization [24]. Consider a bulk superconductor subjected to magnetic field $\mathbf{B}(\mathbf{r})$. Integrating the phase gradient over a closed path we get the phase difference which should be zero modulo 2π in order for the phase to be well defined:

$$2\pi n=\oint\nabla\varphi\cdot d\mathbf{l}=\frac{1}{\hbar}\oint\left(m^{*}\mathbf{v}_{s}+\frac{e^{*}}{c}\mathbf{A}\right)\cdot d\mathbf{l}=\frac{m^{*}}{\hbar e^{*}}\oint\frac{\mathbf{J}\cdot d\mathbf{l}}{\psi_{0}^{2}}+2\pi\frac{\Phi}{\Phi_{0}},$$

where we used $\oint\mathbf{A}\cdot d\mathbf{l}=\int(\nabla\times\mathbf{A})\cdot d\mathbf{s}=\int\mathbf{B}\cdot d\mathbf{s}=\Phi$. Rearranging we get the fluxiod quantization condition:

$$\boxed{\Phi'=\Phi+\frac{m^{*}c}{e*^{2}}\oint\frac{\mathbf{J}\cdot d\mathbf{l}}{\psi_{0}^{2}(\mathbf{r})}=n\Phi_{0}}. \tag{2}$$

Let us explain this concept by considering an Abrikosov vortex [25] as an example. In type II superconductors there is a range of magnetic fields $H\in(H_{c1},H_{c2})$ where the perfect diamagnetism is no longer energetically favorable and flux penetrates the superconductor at limited regions with size $\sim\lambda_{L}$, called the London penetration depth. In the core of these regions superconductivity is suppressed and the cooper pair density n_{s} is reduced from its average value. The suppression of n_{s} is at a region

with characteristic length scale ξ, called the GL coherence length. The magnetic field distribution is realized by circulating currents around the areas where $B \neq 0$, which are called Abrikosov vortices. Considering an integration path far away from the vortex (compared to λ_L), where the circulating current $\mathbf{J}$ will be exponentially small, the total flux Φ will be approximately quantized, $\Phi \approx \Phi_0$, which implies that each vortex carries one flux quantum. However, by taking the integration path closer to the vortex core, the flux enclosed by the integration path is less than the total flux carried by the vortex. This difference in flux is compensated by the non zero circulating current along the path as seen in equation 2.

2.3 The Josephson effect

Placing two superconductors in close proximity to one another, the two wave functions will exponentially decay over the barrier creating an overlap between them. Josephson showed [26] that Cooper pairs will tunnel through, at a rate depending on the difference in the phase $\Delta\varphi = \varphi_2 - \varphi_1$ of the two superconductors. In the presence of magnetic field the phase difference is replaced by the gauge invariant phase difference

$$\gamma \equiv \varphi_2 - \varphi_1 - \frac{2\pi}{\Phi_0}\int_1^2 \mathbf{A}\cdot\mathbf{dl}, \tag{3}$$

where the integration path is taken across the junction. The tunneling rate is given by the so called 'DC Josephson effect':

$$\boxed{I = I_0 \sin\gamma}, \tag{4}$$

where I denotes the super-current through the junction and I_0 is a constant describing the maximal super-current the junction can hold. Above I_0 single electrons, or quasi particle excitations, will also flow through the junction resulting in a final voltage drop V across it. Josephson further showed that the phase difference γ will change in time at a rate proportional to the voltage across the junction. The dependency is known as the 'AC Josephson effect':

$$\boxed{\frac{d\gamma}{dt} = \frac{2eV}{\hbar}}, \tag{5}$$

where $\hbar$ is the reduced Planck constant. Together, the two Josephson equations describe an AC super-current through the junction $I_s = I_0 \sin\left(\frac{2eV}{\hbar}t\right)$ at an angular frequency $\omega = \frac{2eV}{\hbar}$, where the quantum energy $\hbar\omega$ is the energy ascribed to the Cooper pair in the tunneling over the voltage drop V. Below I_0 there is no voltage drop and the current is therefore DC. The two Josephson equations form the basis for the theoretical analysis of the SQUID.

2.4 Non sinusoidal current-phase relations (CPRs)

The Josephson effect can be realized by different junction types. These include S-I-S, S-N-S and S-c-S configurations denoting insulating, normal metal and superconducting constriction respectively. Our SOT devices use the S-c-S configuration also known as Dayem bridges. In his review of different types of weak links, Likharev [27] shows that for a junction of length $L \lesssim \xi$ the CPR is indeed sinusoidal, however, for longer junctions, $L > \xi$, the CPR gradually deviates from the sinusoidal dependency and for $L/\xi \approx 10$ the CPR is approximately linear (see Figure 4). The CPRs calculation assumes a junction with small cross section $a \ll \lambda_L^2$ and that the cooper pair density is constant throughout the electrodes.

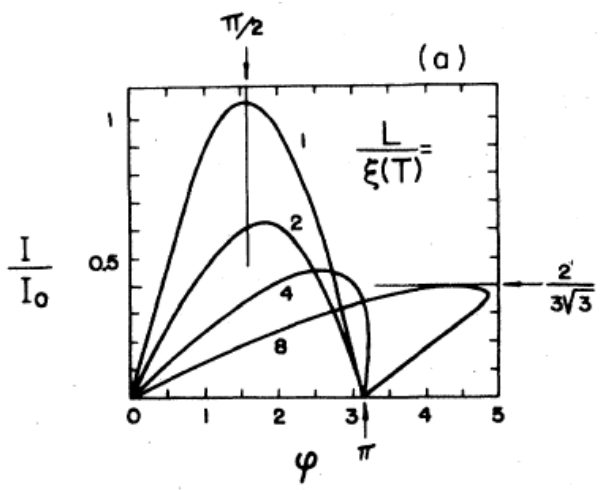

Figure 4: Current phase relations for S-c-S junctions of different lengths L, taken from [27]. For $L = \xi$ the CPR is sinusoidal, but upon increasing L/ξ it eventually becomes linear and multivalued.

2.5 The dc SQUID

The dc SQUID is composed of a superconducting loop, interrupted by two Josephson junctions, or weak links, denoted 1 and 2 as shown in Figure 5a, taken from [17]. A closed line integral of the vector potential $\mathbf{A}$ over a contour passing both electrodes and both junctions gives the flux enclosed in the contour: $\oint \mathbf{A} \cdot d\mathbf{l} = \Phi$. If the electrodes are thick enough compared to λ_L, the magnetic field well inside them is $B \approx 0$ due to the Meissner effect and the integration path inside the electrodes can be chosen such that

$$\mathbf{v}_s^{electrodes} = \frac{\hbar}{m^*}\left(\nabla\varphi - \frac{2\pi}{\Phi_0}\mathbf{A}\right) \approx 0. \tag{6}$$

We can then write

$$\Phi = \oint \mathbf{A}\cdot\mathbf{dl} = \int_{electrodes} \mathbf{A}\cdot\mathbf{dl} + \int_{junctions} \mathbf{A}\cdot\mathbf{dl} \underbrace{\approx}_{\mathbf{v}_s^{electrodes}\approx 0} \frac{\Phi_0}{2\pi}\int_{electrodes} \nabla\varphi\cdot d\mathbf{l} + \int_{junctions} \mathbf{A}\cdot d\mathbf{l}. \tag{7}$$

The single valuedness (modulo 2π) of the phase over a round trip $\int_{electrodes}\nabla\varphi\cdot d\mathbf{l}+\Delta\varphi_1+\Delta\varphi_2 = 2\pi n$ allows us to replace in equation 7 the phase change over the electrodes in favor of the phase differences over the junctions. Along with the definition for the gauge invariant phase difference (equation 3) we can relate the flux to the gauge invariant phase differences over the two junctions:

$$\boxed{\gamma_1+\gamma_2+2\pi\frac{\Phi}{\Phi_0} = 2\pi n}, \tag{8}$$

where both phase differences are taken counterclockwise. The maximal super-current through the device is the sum of the maximal super-currents through both branches $I_c = I_{0,1}\sin\gamma_1 - I_{0,2}\sin\gamma_2$ (the minus sign is because the γs were both defined counterclockwise). This so called critical current I_c is therefore a function of the total flux Φ penetrating the loop. Assuming identical junctions $I_{0,1} = I_{0,2} \equiv I_0$ and using trigonometric identities we find:

$$\boxed{I_c = 2I_0\left|\cos\frac{\pi\Phi}{\Phi_0}\right|},$$

which describes the maximal dissipationless current through the SQUID as function of the magnetic flux penetrating it, see Figure 5b. The total magnetic flux is the sum of the flux due to externally applied field Φ_a and the flux due to screening currents $\Phi_s = LJ$, where $L = L_g + L_k$ is the total loop inductance, composed of both geometric and kinetic inductances L_g and L_k respectively [28] and J denotes the circulating current in the SQUID loop. The dependency of the maximal dissipationless current on the *externally* applied flux, $I_c(\Phi_a)$, is similar, but distorted due to the screening. Whenever $\Phi_a = n\Phi_0$, however, the circulating current is zero and $\Phi_{tot} = \Phi_a$, so that the points of $I_c(n\Phi_0)$ does not depend on the inductance.

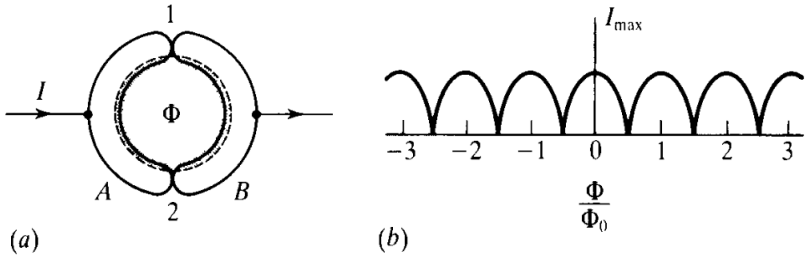

Figure 5: (**a**) A schematic of a SQUID and (**b**) the resulting $I_c(\Phi)$ interference pattern. Figure taken from [17].

The dependency of I_c on the flux is what makes the SQUID a magnetometer. By measuring changes in the critical current the flux can be inferred. In practice the critical current is not directly measured and instead, the SQUID is usually current biased above I_c in the so called voltage state, where part of the current through the junctions is due to unpaired electrons. The total current through the SQUID in the voltage state is also modulated with flux in a similar fashion to $I_c(\Phi)$. The response $|dI/d\Phi|$ of the SQUID is similar to $|dI_c/d\Phi|$, which is highest around $\Phi = (n+1/2)\Phi_0$. However, around these flux value the response changes sign, resulting in a highly non linear magnetometer. For this reason, the best sensitivity which also ensures linearity of the device is around $\Phi \approx (1/4+n/2)\Phi_0$. A very useful analysis of SQUIDs in the voltage state was done by Tesche and Clarke [29].

2.6 Thin film SQUIDs with Dayem bridges

In thin film SQUIDs the SC electrodes can have a thickness of order λ_L, thus there is no path in the electrodes along which $\mathbf{v}_s = 0$. Furthermore, as mentioned above, the CPR can be far from sinusoidal for certain configurations. Under these conditions the assumptions used to derive the Josephson equations no longer hold and one usually resorts to the GL theory to describe the SQUID as a whole. Theoretical and experimental analysis for the CPRs and the resulting $I_c(\Phi)$ in μm diameter SQUIDs with of sub μm Dayem bridges was given by [30] using GL theory numerical calculations. In these SQUIDs, it seems, the phase gradients and suppression of the Cooper pair density is not restricted to the junction, but extends throughout the SQUID, which further influences the CPRs. It was found both theoretically and experimentally that the CPRs for certain junctions are highly non sinusoidal, especially ones that are long compared to ξ. This results in a more triangular shaped interference pattern $I_c(\Phi)$ with smaller modulation depth which is defined as [29]

$$\Delta I_c \equiv \frac{I_c^{max} - I_c^{min}}{I_c^{max}},$$

where $I_c^{max} \equiv \max_\Phi (I_c(\Phi))$ and $I_c^{min} \equiv \min_\Phi (I_c(\Phi))$. With this definition the modulation depth ranges from 0 to 1 for different SQUIDs. Roughly speaking, the smaller the modulation depth the smaller the response of the SQUID which corresponds to a degraded performance as a magnetometer. The influence of the CPR on the modulation depth was investigated by Duzer and Tsang [31] who show that sinusoidal CPR yields the optimal modulation depth. To optimize the SQUID's performance one should thus decrease the junctions' cross section and length to minimum.

The modulation depth is affected, however by many other factors, amongst them are critical current asymmetry and inductance. A very important factor that influences the modulation depth is the dimensionless screening parameter, defined as [29]:

$$\beta_L \equiv \frac{2I_0 L}{\Phi_0}.$$

A numerical calculation of the dependence of $I_c(\Phi)$ for a symmetric SQUID, taken from [29], is given in Figure 6 and shows that higher β_L corresponds to lower ΔI_c. The modulation depths for a few selected β values are 1, 0.5 and 0.3 for $\beta_L = 0$, 1 and 2 respectively.

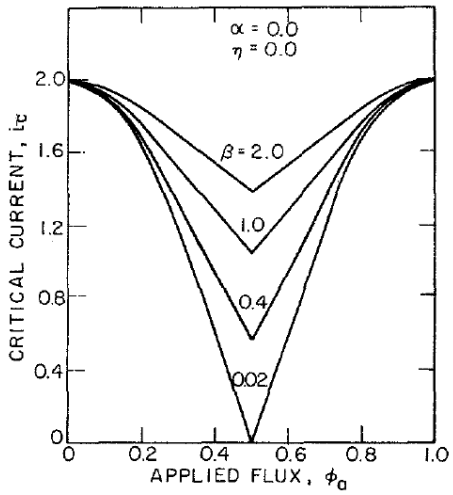

Figure 6: $I_c(\Phi)$ dependence for a conventional symmetric SQUID, taken from [29]. Higher screening parameter β_L corresponds to lower modulation depth ΔI_c.

3 MSOT fabrication

The MSOT fabrication is done in three main steps (see Figure 3). First, a quartz tube is pulled into a sharp pipette using a commercial Sutter Instruments 'P-2000' micropipette puller. The macroscopic part of the tube (excluding the taper) is then deposited with Au contacts and later covered with thick In layer applied using a soldering iron. Lastly, the tip is deposited with SC thin films using a thermal evaporator.

3.1 Step 1 - Pulling

The quartz tubes used for the MSOT have four grooves (see Figures 3 and 22) that create the shading required for the four leads. They are fabricated on demand by Friedrich & Dimmock, Inc. Different pulling parameters can be used for different desired tip diameters, ranging from ~170 to 100 nm outer diameter and less (see also section 8.2).

3.2 Step 2 - Au and In leads

After the tube has been pulled into a sharp pipette the contacts are deposited. An 8 nm Cr adhesion layer followed by a 50 nm Au layer are deposited on two opposite sides of the tube, keeping the taper shaded using a mask. One might suggest to do a four sides deposition for the four required contacts,

but this might easily result in shorting two adjacent leads together. Instead, depositing only two sides creates two well formed leads, denoted 1 and 3, and another two leads, denoted 2 and 4, each of which is divided in two halves. The Au layer has a smooth edge that ensures no shading will occur when depositing the Pb leads. It has however high resistance of order 20 Ω which is unwanted due to a reason that will be explained in section 4.1. To reduce it, a thick layer (~500 μm) of In is applied by hand using a soldering iron. The In layer also uses to short together both halves of the two parted Au contacts (2 and 4) making each of them an effective single contact as required.

3.3 Step 3 - Pb deposition

Finally Pb is deposited on the quartz taper, overlapping the Au contacts. This is done in high vacuum, with a base pressure of 2×10^{-7} Torr. The high surface mobility of the Pb atoms on the quartz results in the formation of islands that will only form a continuous film at high thicknesses. To reduce the Pb atoms mobility the quartz tip is cooled prior to deposition using a continuous flow liquid ^{4}He cryostat that allows in-situ rotation. The ^{4}He is directly cooling a brass block with a narrow slit that accommodates the tip. The thermal contact between the brass block and the tip is done by introducing ^{4}He exchange gas into the evaporator chamber (see also appendix 8.3) prior to each of the three depositions (15 minutes at 5×10^{-3} Torr, 6 minutes at 5×10^{-3} Torr and 6 minutes at 1×10^{-2} Torr before the first, second and third depositions respectively). After the tip is cooled the exchange gas is removed and the pressure is lowered back to base pressure prior to each of the depositions. Each of the two MSOT's sides is deposited with 16 nm Pb thin film with the tip axis at ± 110 degrees with respect to the source-tip axis, and lastly the MSOT's ring is faced toward the source and deposited with 12 nm Pb thin film. The leads deposition is done with the tip at the same orientation as in the Au leads deposition to prevent shorting of two adjacent Pb leads by the Au. Once the deposition is over the MSOT is left to slowly warm up to room temperature which takes about 80 minutes. It is then imaged by a scanning electron microscope (SEM) for quality control.

4 Measurement Setup

Bulk Pb superconductivity occurs below a critical temperature of 7.2 K. This allows operation of the MSOT at liquid ^{4}He temperatures (4.2 K). The MSOT is mounted on a 'tip holder', physically holding it in place and electrically connecting the tip to the external circuit via four metallic springs. The tip holder is put inside a vacuum can which is pumped to a pressure of about 1×10^{-2} mBar and then submerged into liquid ^{4}He. After the setup has reached 4.2 K ^{4}He exchange gas is introduced into the vacuum can at pressure up to ~2/3 Bar. The exchange gas keeps the MSOT at constant temperature and prevents it from heating when it is in the dissipative state. Since I_c is temperature dependent, heating of the SQUID would result in a hysteretic current-voltage curve, an issue that was addressed by [30].

The electrical circuit used to bias and measure the MSOT is presented in Figure 7b. It is a generalization of the more conventional 2 terminal, 2 junction SOT circuit, shown in Figure 7a for reference. Let us first describe the simpler SOT circuit. The SOT is biased using a current source (bias voltage V_B is series with a large cold resistor R_B of order a few kΩ) with a shunt resistor R_S of order few Ω in parallel to the SOT. This results in a load line with a negative slope which allows non hysteretic operation for our SOTs which usually have negative differential resistance $R_D \equiv dV_{SOT}/dI_{SOT} < 0$. The SOT is in series with a parasitic resistance R_P usually of order 1 Ω which is due to contact and wire resistances. When the SOT is in the superconducting state most of the current flows through it and only a small fraction flows through the shunt resistor. In the dissipative state, however, the resistance of the SOT increases thus reducing the current through it in favor of the current through the shunt resistor. The current through the SOT is measured using a cold Series SQUID Array Amplifier (SSAA) [9, 12, 32] consisting of 100 dc SQUIDs operated in a FLL mode. Along with a feedback resistor R_{FB} of order few kΩ it acts as a current to voltage pre-amplifier with typical current noise of about 2.5 to 10 pA$/\sqrt{\text{Hz}}$ and transfer function of order few 10 kΩs which is calibrated per setup allowing to infer I_{SOT} from the measured V_{FB} by $I_{SOT} = V_{FB}/\eta R_{FB}$, where η denotes the turn ratio between an input and a feedback coil inductively coupled to the SSAA.

In the MSOT circuit a second biasing terminal is added as well as an extra measured current using a second SSAA. The three degrees of freedom available for operating the MSOT are V_{B1}, V_{B2} and B_a which denote the bias voltage on terminal 1, the bias voltage on terminal 2 and the externally applied magnetic field respectively, generated by a SC coil. A third bias terminal can in principle be introduced, allowing for a fourth degree of freedom V_{B4}, however in the data presented herein it is kept floating.

Both the DC current through the MSOT and the white current noise are simultaneously measured. The white noise circuit is described in Figure 7c and the measurement is done in the following manner (see also section 8.4.2). The time domain raw signal $V_{FB}(t)$ is filtered around 10 kHz, amplified, rectified using a diode, amplified again and finally the output voltage is measured by averaging over ~1 ms to get the DC component of the signal, denoted V_{diode} which is proportional to the 10 kHz noise amplitude. The proportionality constant is determined by a calibration measurement comparing the diode output DC average with the V_{FB} 10 kHz component measured by a spectrum analyzer.

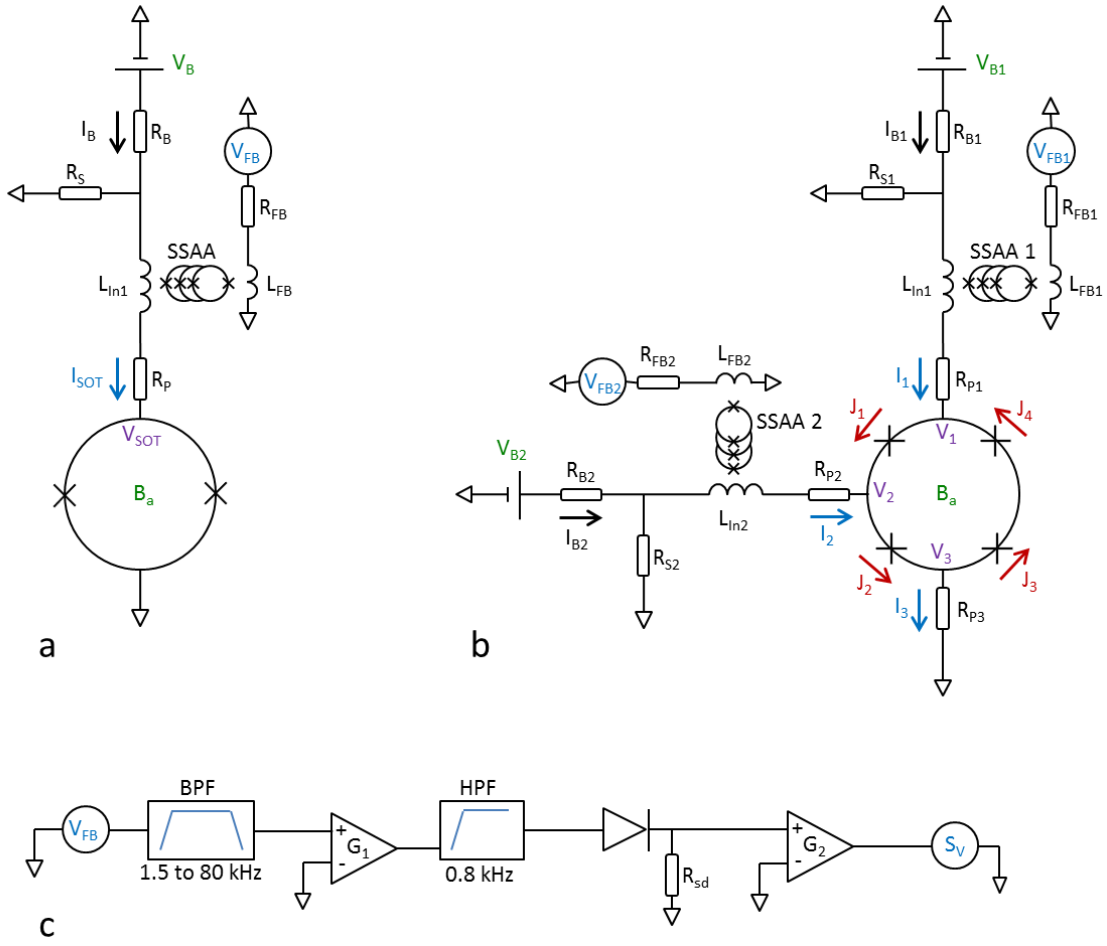

Figure 7: Electrical circuit schematics: (**a**) The 2 terminal SOT measurement circuit, given as a reference, (**b**) the MSOT circuit and (**c**) white noise measurement circuit. The values of the passive components used in the MSOT circuit are $R_{B1} = 5$ kΩ, $R_{B2} = 3$ kΩ, $R_{S1} = R_{S2} = 5$ Ω, $R_{FB1} = 3$ kΩ and $R_{FB2} = 1$ kΩ. The turn ratios on the input to feedback coils of the two SSAAs are $\eta_1 = 8.57$ and $\eta_2 = 8.56$ and the parasitic resistances calculated from the measurement are $R_{P1} + R_{P3} \approx R_{P2} + R_{P3} \approx 2\ \Omega$.

4.1 MSOT load lines

As explained above, the two terminal SOT bias circuit results in a load line appropriate for operating SQUIDs with negative differential resistance. We shall address this point more carefully here, generalizing it to the MSOT circuit. The current through the SOT is given by [33]:

$$I_{SOT} = \frac{R_S}{R_P + R_S} I_B - \frac{1}{R_P + R_S} V_{SOT},$$

where $I_B = \frac{V_B}{R_B}$. This equation describes the crossing point of the SOT *intrinsic* $I_{SOT}(V_{SOT})$, so called I-V curve, with a 'load line' determined by the shunt and parasitic resistances of the probing *circuit*. Voltage bias corresponds to a vertical load line, current bias to a horizontal one and our SOT circuits

gives something in between with a slope of $-(R_S+R_P)^{-1}$. A SOT with negative differential resistance R_D requires a circuit with a steep enough load line, otherwise the crossing point will not be single valued and the measured I-V curve will show hysteretic behavior. The condition for single valued crossing is $R_S+R_P<|R_D|$ over the whole I-V curve. The load line equation for the SOT is also used to calculate the intrinsic $I_{SOT}(V_{SOT})$ curves from the measured $I_{SOT}(I_B)$ curves.

Considering now the MSOT, a straight forward calculation gives the equivalent dependency (see Figure 7b for the notation):

$$I_1=\frac{R_{S1}R_2}{\tilde{R}^2}I_{B1}-\frac{R_{S2}R_{P3}}{\tilde{R}^2}I_{B2}-\frac{R_2}{\tilde{R}^2}\Delta V_1+\frac{R_{P3}}{\tilde{R}^2}\Delta V_2$$

$$I_2=\frac{R_{S2}R_1}{\tilde{R}^2}I_{B2}-\frac{R_{S1}R_{P3}}{\tilde{R}^2}I_{B1}-\frac{R_1}{\tilde{R}^2}\Delta V_2+\frac{R_{P3}}{\tilde{R}^2}\Delta V_1$$

where we defined $\Delta V_1\equiv V_1-V_3$, $\Delta V_2\equiv V_2-V_3$, $R_1\equiv R_{S1}+R_{P1}+R_{P3}$, $R_2\equiv R_{S2}+R_{P2}+R_{P3}$ and $\tilde{R}^2\equiv R_1R_2-R_{p3}^2$. The bias currents are simply $I_{Bi}=\frac{V_{Bi}}{R_{Bi}}$. Note that the bias lines in the circuit are symmetric, therefore we get the second equation from the first by interchanging the indices $1\longleftrightarrow 2$. These equations describe two 'load plains', which are a generalization of the load line to the 2d $\{\Delta V_1,\Delta V_2\}$ parameter space. The MSOT intrinsic I-Vs are two surfaces I_1 and I_2 in the parameter space, for constant magnetic field. The intercept of each of the load planes with the corresponding I-V surface is a 1d curve. The two curves, however, are not independent and the point in the parameter space that is being probed is given by the intercept of the projection of the two curves onto the $\{\Delta V_1,\Delta V_2\}$ plane.

To simplify this we reduce the two 2d equations into one 1d equation by plugging ΔV_2 from the second equation into the first one. This gives:

$$I_1=\frac{R_{S1}}{R_1}I_{B1}-\frac{R_{P3}}{R_1}I_2-\frac{1}{R_1}\Delta V_1, \tag{9}$$

and from the circuit symmetry $1\longleftrightarrow 2$ we get:

$$I_2=\frac{R_{S2}}{R_2}I_{B2}-\frac{R_{P3}}{R_2}I_1-\frac{1}{R_2}\Delta V_2. \tag{10}$$

Setting, for example, $I_2=0$ in equation (9) it reduces to the SOT load line, with the trivial replacements $R_P\to R_{P1}+R_{P3}$ and $R_S\to R_{S1}$ (see above definition for R_1). In the more general case of $I_2\neq 0$, the load line is simply shifted up or down, not affecting its slope. In conclusion, for non hysteretic behavior of the MSOT R_S and R_P must satisfy:

$$\boxed{R_{S1}+R_{P1}+R_{P3}<|R_{D1}|\equiv\left|\frac{\partial\Delta V_1}{\partial I_1}\right|}$$

and

$$\boxed{R_{S2}+R_{P2}+R_{P3}<|R_{D2}|\equiv\left|\frac{\partial\Delta V_2}{\partial I_2}\right|},$$

which is a trivial generalization for the SOT's condition.

Finally, the following equations (11) and (12) allow calculating the intrinsic $I_i(\Delta V_1, \Delta V_2)$ surfaces from the measured $I_1(V_{B1}, V_{B2})$ and $I_2(V_{B1}, V_{B2})$. An example of the measured $I_1(V_{B1}, V_{B2})|_{B_a=0}$ is given in Figure 10.

$$\boxed{\Delta V_1 \equiv V_1 - V_3 = R_{S1}\left(\frac{V_{B1}}{R_{B1}} - I_1\right) - (R_{P1} + R_{P3})I_1 - R_{P3}I_2} \tag{11}$$

$$\boxed{\Delta V_2 \equiv V_2 - V_3 = R_{S2}\left(\frac{V_{B2}}{R_{B2}} - I_2\right) - (R_{P2} + R_{P3})I_2 - R_{P3}I_1} \tag{12}$$

5 Theoretical DC analysis of the MSOT

5.1 The basic principle of operation

We shall start the theoretical analysis by giving a simple intuitive explanation of the basic principle by which shifting of the interference pattern is achieved. A simulation of the MSOT in the DC regime, i.e. below I_c gives both the total critical current I_c through the device but also the currents through each of the junctions J_i which allows better understanding of MSOT behavior. I_i and J_i denote the current through terminal i and junction i of the MSOT respectively (see notation in Figure 7). We define the asymmetry parameters a_i for the critical currents in the junctions by $I_{0,i} = a_i I_0$ and take them all to be of value 1 for simplicity.

For a given V_{B2} value the curve $I_{c1}(B_a)$ has the shape of an absolute value of a cosine with a period of $\Delta B_a = \Phi_0/A$. Upon changing V_{B2} this interference pattern shifts and its maximum follows a one dimensional (1d) trajectory in the space $\{B_a, V_{B2}\}$. Figure 8 shows an illustration of such a trajectory for one of the maxima. Starting with negative values of V_{B2} and slowly increasing it, the trajectory goes through five different points denoted (a) to (e) in the Figure. At point (a) where $I_2 = -2$ and $I_{c1}^{max} = 2$, the current injected at terminal 1 splits between the left and right branches of the MSOT driving junctions 1, 3 & 4 into criticality simultaneously. Increasing V_{B2} results in the increase of I_2 from -2, passing through point (b) and reaching point (c), where nothing changes, except that J_2 increases continuously from -1 to 1. Note that I_{c1}^{max} still equals 2 and all three currents through junction 1, 3 & 4 remain constant and equal to 1, fixing the total critical current I_{c1}. Junction 2 however does not reach criticality between points (a) and (c) (except exactly at these points). Increasing V_{B2} further the trajectory goes through point (d) and reaches point (e) where I_2 is positive, and junction 2 is at criticality with $J_2 = const = 1$. J_1 however is smaller than 1 and the criticality on the left MSOT branch is due to junction 2 and not 1. This happens because $J_2 = I_2 + J_1$ and given a certain current $I_2 > 0$, J_1 has to be smaller than 1, since $J_2 > 1$ is not allowed, otherwise the the MSOT is in the voltage state. At point (e) the story ends because increasing I_2 further will drive the MSOT into the voltage state. A similar argument holds for the other end of the trajectory, at point (a).

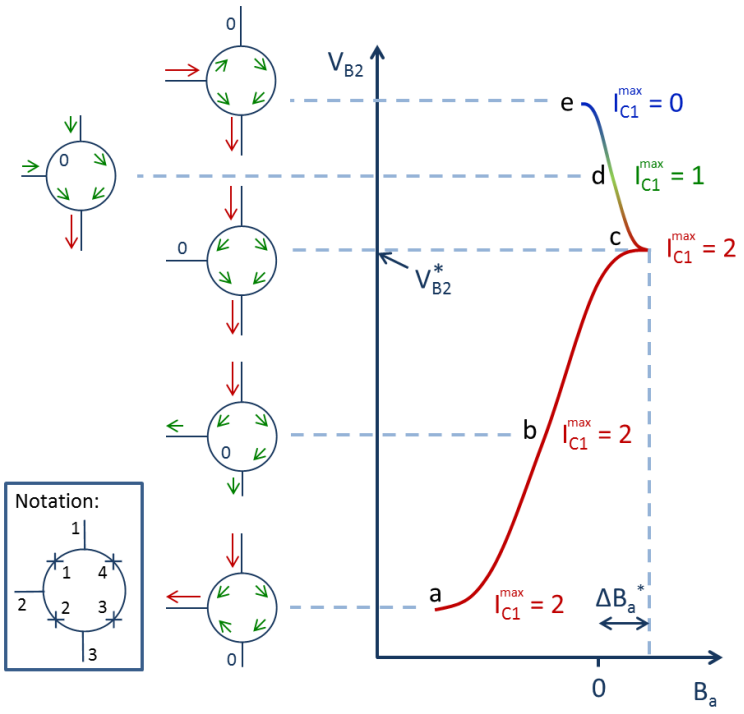

Figure 8: An illustration of the trajectory of the maximal critical current through terminal 1 in the $\{B_a, V_{B2}\}$ space. The currents through all four junctions and through terminal 1 and 2 are shown for selected points on the trajectory. The magnitude of the currents is encoded in both the color and length of the arrows. All junctions are assumed to have the same critical current $I_{0,i} = I_0$ and the currents shown are normalized to it. The trajectory is ultimately determined by the current-phase relation of the MSOT's junctions 2 (points a through c) and 1 (points c through e).

Equipped with the knowledge of all four J_i along the trajectory we can now explain its *shape*. We consider the following generalization of equation 8 for the case of four junctions in series along the ring:

$$\sum_{i=1}^{4} \gamma_i + 2\pi \frac{\Phi_{tot}}{\Phi_0} = 2\pi n, \tag{13}$$

where γ_i is the gauge invariant phase difference along junction i and all phase differences are defined counterclockwise. As discussed above, $\Phi_{tot} = \Phi_a + \Phi_s$ is the total flux in the SQUID composed of the externally applied flux Φ_a and the effective flux induced by screening currents $\Phi_s = LJ = (L_k + L_g)J$, where L_k and L_g are the total kinetic and geometric inductances of the four parts of the ring. Here $J \equiv \frac{1}{4}\sum_i J_i$ is defined as the circulating current and we assumed no inductance asymmetry. We note that for the MSOT (as for the SOT) the kinetic inductance dominates, $L_k \gg L_g$. The small ring area results in small geometric inductance whereas the small cross section a of the Pb thin film on the ring, comparable to ξ^2 results in high current densities therefore high kinetic inductance [1, 12, 34].

Along the points (a) to (c) the currents J_1, J_3 and J_4 are constant and thus so are their phases γ_1, γ_3 and γ_4. This, along with equation 13 allows us to write

$$\gamma_2 \sim \Phi_{tot}.$$

Now, I_1 is constant along points (a) to (c), which means that I_2 depends linearly on V_{B2}. Putting it all together we get:

$$\boxed{V_{B2} \sim I_2 = J_2 - J_1 \sim \sin\gamma_2 \sim \sin\Phi_{tot} \approx \sin\Phi_a} \ (\text{for } -I_c < I_2 < I_c),$$

where in the last step we neglected the inductance L for simplicity. The basic principle for shifting the interference pattern is now clear: By controlling V_{B2} we control I_2, which in turn determines γ_2. By changing only γ_2 and keeping the field B_a constant, equation 13 suggests that the other phases would change, therefore changing the corresponding currents, resulting in $I_{c1} < I_{c1}^{max}$. Therefore, in order to stay on the I_{c1}^{max} trajectory, the change in γ_2 must be compensated with a change in the flux Φ_a which explains the shift of $I_c(\Phi_a)$.

The result is even more meaningful than this. The trajectory of the maximal I_{c1} from points (a) to (c) follows the current-phase relation of junction number 2 (assuming negligible inductance). This possibly allows probing the CPR for the Dayem bridges used in our SOTs.

As for the rest of the trajectory, i.e. points (c) to (e), a similar argument can be given. Along this part of the trajectory, the constant currents are J_2, J_3 and J_4 and V_{B2} controls the phase difference γ_1. We can thus write:

$$\gamma_1 \sim \Phi_{tot}$$

and

$$V_{B2} \sim I_2 = J_2 - J_1 \sim -\sin\gamma_1 \sim -\sin\Phi_{tot} = \sin(-\Phi_{tot}),$$

so that this part of the trajectory is determined by the CPR of junction number 1.

5.1.1 The $I_c(\Phi_a, V_{B2})$ surface, beyond the $V_{B2}(\Phi_a)|_{I_c^{max}}$ curve

Above the qualitative behavior of the *maximal* critical current curve $V_{B2}(\Phi_a)|_{I_c^{max}}$ is explained. To understand the behavior of the full $I_c(\Phi_a, V_{B2})$ surface (e.g. Figure 12) we consider the following argument. Since $I_1 = J_1 - J_4$, it is a function of the phase differences γ_1 and γ_4. In the setup where terminal 4 is floating, $J_3 = J_4 \ \Rightarrow \ \gamma_3 = \gamma_4$. Now, the relation $\sum\gamma_i + \pi\Phi_{tot}/\Phi_0 = 2\pi n$ means we can replace the dependency of I_1 on γ_1 and γ_4 with a dependency on γ_1 and the sum $\gamma_2 + \pi\Phi_{tot}/\Phi_0$, so that $I_1 = I_1(\gamma_1, \gamma_2 + \pi\Phi_{tot}/\Phi_0)$. We now differentiate between two cases: (1) Junction number 1 is the limiting junction for the dissipationless current on the MSOT's left branch and (2) The critical current is limited by junction 2. These cases correspond to points (a)-(c) and (c)-(e) in Figure 8 respectively. To get the critical current in case (1) we maximize I_1 with respect to γ_1. The critical current is now

independent on γ_1:

$$I_{c1} = I_{c1}\left(\gamma_2 + \pi\Phi_{tot}/\Phi_0\right).$$

This simply means that by simultaneously changing $\gamma_2 \to \gamma_2 + \delta$ and $\Phi_{tot} \to \Phi_{tot} - \delta \times \Phi_0/\pi$ the critical current is unaffected: $I_{c1} \to I_{c1}$. This applies not only to the maximal critical current I_{c1}^{max}, but also to the minimal critical current I_{c1}^{min} as well as to all intermediate values of I_{c1}. Since $I_2 = J_2 - J_1$ and $J_1 = J_1(\gamma_1)$ is determined by the maximization condition, we have

$$\boxed{I_2 \sim J_2 \sim \sin\gamma_2 \sim \sin\left(-\pi\Phi_{tot}/\Phi_0\right)}.$$

This describes a very simple shift of the interference pattern $I_c(\Phi_a)$ upon changing I_2.

In the second case, the maximization of I_1 is done with respect to γ_2, which leaves $I_{c1} = I_{c1}(\gamma_1, \Phi_{tot})$ and does not allow using a similar argument to that of the first case. Indeed, as demonstrated experimentally and by simulation (see below), $I_c(\Phi_a)$ does not remain constant in this region upon any combination of changes in Φ_a and I_2.

5.2 DC analysis

Calculating the critical current of the MSOT is done numerically. There is however a long way we can go analytically. This is done in three steps: first, we apply the Kirchhoff constraints of the circuit and solve them. Second, we use the Lagrange multipliers method to maximize the current and find $\gamma_1(\gamma_2, \gamma_3)|_{I_{c1}}$. Lastly we map the phases space to the external circuit's parameter space, i.e. $\{\gamma_1, \gamma_2, \gamma_3\} \to \{I_1, V_{B2}, B_a\}$, to get $I_{c1}(B_a, V_{B2})$. We present here the mathematical procedure in short. For the full details, see appendix 8.5. We stress that the following is only valid for $I \leq I_c$, i.e. as long as the tip is in the SC state.

5.2.1 Step 1 - Kirchhoff equations

The five (linear) Kirchhoff equations describing the circuit (see Figure (7)) are:

1. $0 = V_{B1} - I_{B1}R_{B1} - (I_{B1} - I_1)R_{S1}$
2. $0 = V_{B1} - I_{B1}R_{B1} - I_1R_{P1} - I_3R_{P3}$
3. $0 = V_{B2} - I_{B2}R_{B2} - (I_{B2} - I_2)R_{S2}$
4. $0 = V_{B2} - R_{B2}I_{B2} - R_{P2}I_2 - R_{P3}I_3$
5. $0 = I_1 + I_2 - I_3$

We use them to find

$$I_2(I_1, V_{B1}) = -\left(\frac{R_{S1}}{R_{P3}} + \frac{R_{P1}}{R_{P3}} + 1\right)I_1 + \frac{R_{S1}}{R_{P3}}\frac{V_{B1}}{R_{B1}} \tag{14}$$

5.2.2 Step 2 - Lagrange multipliers method

We now face a maximization problem, involving a set of non linear equations due to the current phase relations of the Josephson junctions. We address this problem using the Lagrange multipliers method. We first go to dimensionless variables:

$$i_i \equiv \frac{I_i}{I_0},\ j_i \equiv \frac{J_i}{I_0},\ \phi \equiv \frac{\Phi}{\Phi_0},\ \beta_L \equiv \frac{2I_0 L}{\Phi_0},$$

where I_0 is the critical current through each one of the junctions, assuming symmetric junctions. We wish to maximize i_1 with the following constraints. The first accounts for the fact that terminal 4 is floating:

$$i_4 = 0 \tag{15}$$

The second is

$$\sum_i \gamma_i + 2\pi\phi_{tot} = 0, \tag{16}$$

where $\phi_{tot} = \phi_a + \phi_s$ and $\phi_s = j\beta_L/2$, where we define $j \equiv \frac{1}{4}L\sum_i j_i$ to be the dimensionless circulating current. The last constraint is

$$i_2\left(i_{B1}, i_1 = j_1 - j_4\right) - \left(j_2 - j_1\right) = 0, \tag{17}$$

which involves the following: $0 = i_2 - (j_2 - j_1)$ and $0 = i_1 - (j_1 - j_4)$. The variable V_{B1} appears in this constraint multiplied by R_{S1} so it will eventually fall when taking the derivative. We will then be left only with variables intrinsic to the MSOT. The Lagrangian is therefore:

$$\mathscr{L} = i_1 + \lambda_1 i_4 + \lambda_2\left(\sum_i \gamma_i + 2\pi\phi_a + \pi\beta j\right) + \lambda_3\left(i_2\left(i_{B1}, i_1\right) - i_2\right), \tag{18}$$

in which we substitute the currents through the MSOT terminals $i_i \to j_i - j_{\mod 4(i-1)}$ and the currents through the junctions $j_i \to a_i \sin\gamma_i$. The a_i are defined through $I_{0,i} = a_i I_0$ thus denote the four junctions critical current asymmetry. We now have 7 unknowns: four phases γ_i and three Lagrange multipliers λ_j. We take the gradient in the phases parameter space and equate to zero to get four equations:

$$\nabla_{\gamma_i}\mathscr{L} = 0.$$

Using three of these equations we can solve for the Lagrange multipliers λ_j. We then plug them into the fourth equation to get $\gamma_1\left(\gamma_2, \gamma_3\right)|_{I_{c1}}$:

$$\boxed{\sum_i \frac{1}{a_i \cos\gamma_i} + \pi\beta_L = 0}. \tag{19}$$

The constraint $i_4 = 0$, means $\sin\gamma_4 = \sin\gamma_3$ which can be used to eliminate γ_4 from equation (19). This equation now describes a relation between γ_1, γ_2 and γ_3 at the critical current i_{c1}. This can be pictured as a surface $\gamma_1(\gamma_2,\gamma_3)|_{i_{c1}}$. Given a pair $\{\gamma_2,\gamma_3\}$, one can determine the value of γ_1 that will give the maximum for i_1. This dependency of the critical current on two intrinsic MSOT parameters can be mapped to the dependence $i_{c1}(B_a,V_{B2})$ which is given in the external circuit parameter space. Every point on the surface $\gamma_1(\gamma_2,\gamma_3)|_{i_{c1}}$ corresponds to a point on the critical current surface $I_{c1}(B_a,V_{B2})$. The experimental result for $I_{c1}(B_a,V_{B2})$ is presented in Figure 12.

5.2.3 Step 3 - Mapping to the circuit parameter space

The mapping of $\{\gamma_1,\gamma_2,\gamma_3\} \rightarrow \{i_1,V_{B2},B_a\}$ allows us to map $\gamma_1(\gamma_2,\gamma_3)|_{i_{c1}} \rightarrow i_{c1}(B_a,V_{B2})$. We use the following procedure: the phases γ_i give the currents through the junctions $j_i = a_i\sin\gamma_i$ and thus the currents through the three terminals $i_i = j_i - j_{(i-1) \mod 4}$. By using the Kirchhoff equations we can determine $V_{B2}(I_1,I_2) = \frac{R_{P3}}{R_{S2}}R_{B2}I_1 + \left(1+\frac{R_{P2}+R_{P3}}{R_{S2}}\right)R_{B2}I_2$ and by using equation 16 we get the applied flux $2\pi\phi_a = -\sum_i\gamma_i - \pi\beta_L j = -\sum_i\left(\gamma_i + \frac{1}{4}\beta_L a_i\sin\gamma_i\right)$. A simulation of $I_{c1}(B_a,V_{B2})$ is presented in Figure 14.

6 Results

6.1 Measurement

The characterization of the MSOT was done in two main steps. First, the current through terminals 1 & 2 was measured, probing the full relevant parameter space, i.e. $I_i(V_{B1}, V_{B2}, B_a), \quad i = 1,2$. This was done by applying DC bias to the tip in all V_{B1}, V_{B2} and B_a and measuring simultaneously the DC currents I_i^{DC} and the 10 kHz (white) noise on this current, $S_i(10\,\text{kHz})$. The noise measurement was done using the circuit described in section 4 above. Since the parameter space is large the measurement was done using a Digital to Analog Converter (DAC) and an Analog to Digital Converter (ADC). Every point in the parameter space took ~$2ms$ to acquire and the total of $360 \times 300 \times 300 \approx 3 \times 10^7$ points took ~24 hours. This measurement allowed calculating the MSOT response dV_{FBi}/dB_a on both terminals $i = 1,\ 2$ and also its flux noise $S_{\Phi i}^{1/2} \sim S_{Vi}^{1/2} / \frac{dV_{FBi}}{dB_a}$ in the 3d parameter space. The second main step of the measurement was to more carefully measure the MSOT's noise spectra using a spectrum analyzer. Since measuring low frequency spectra takes a long time we cannot afford taking it over the full parameter space. Instead, using the flux noise data from the previous measurement we find the point in $\{V_{B1}, V_{B2}\}$ space with the lowest noise for every field B_a. These so called 'Working Points' (WPs) form a 1d trajectory in the 3d parameter space. Spectra was then taken with the MSOT subject to the parameters on this trajectory. We will now present the results of both these steps.

6.2 Mapping of the 3d parameter space

6.2.1 Current-Voltage (I-V) curves

Figure (9) shows the basic building block of the MSOT characteristics, namely I-V curves at varying magnetic fields, for constant $V_{B2} = 0.228\,V$. The change in the I-V curve due to the applied magnetic field is what ultimately makes the SQUID a magnetometer. Figure 10 also shows I-V curves but this time as a function of both V_{B1} and V_{B2} and at a constant magnetic field $B_a = 0$. We can now take a few cross sections of the 3d data to see the MSOT's behavior.

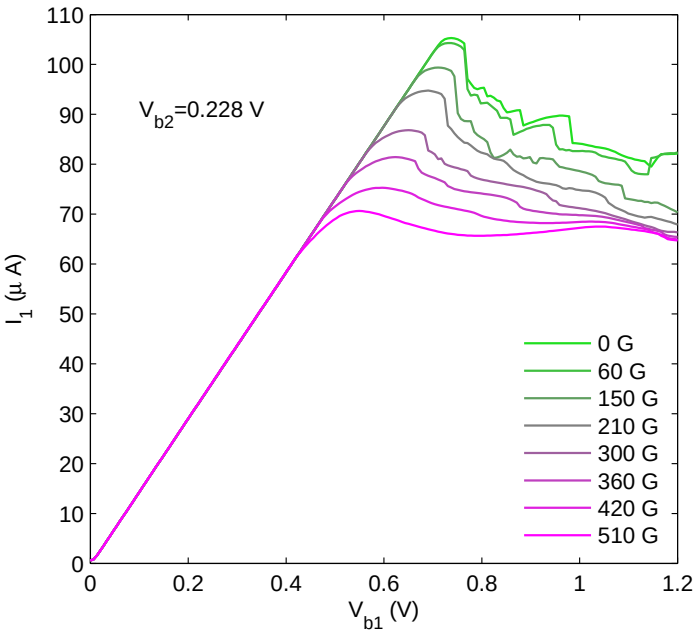

Figure 9: Current through terminal 1 as function of bias voltage on the same terminal. The different curves correspond to different applied magnetic fields, from 0 to 510 G, which corresponds to $\sim \Phi_0/2$. The bias on terminal 2 is constant and set to 0.228 V.

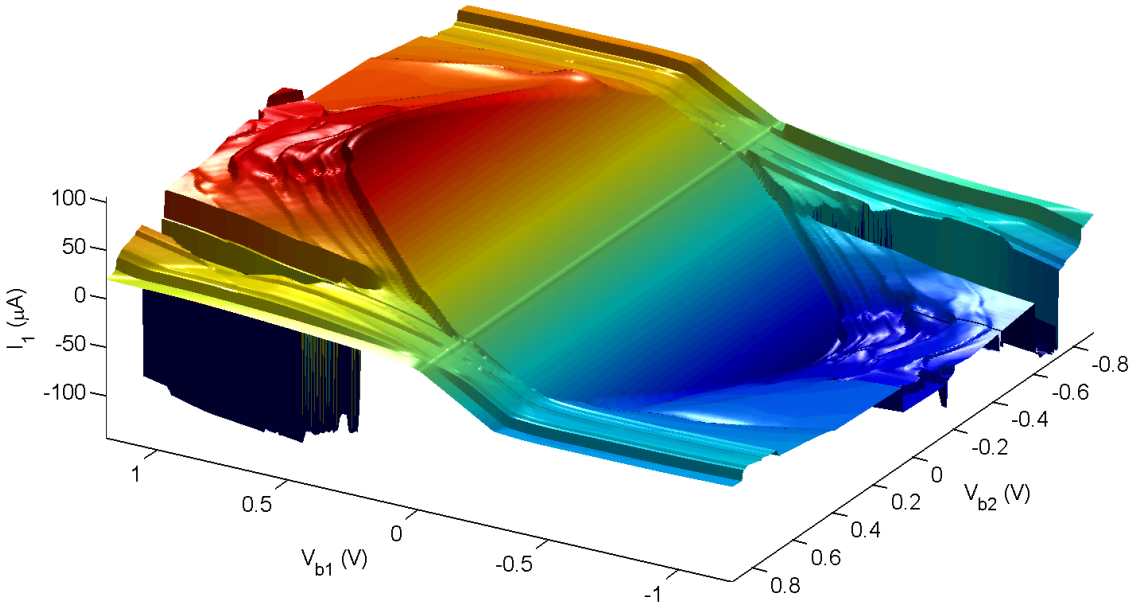

Figure 10: Current through terminal 1 as function of both bias voltages V_{B1} and V_{B2}, at zero field. The plane in the middle corresponds to the SC state. The vertical plains at $V_{B2} \approx \pm 0.7\,V$ are an artifact of the measurement and not real features of the device.

6.2.2 Interference patterns - asymmetry and time reversal considerations

Figure 11 shows different parameters of the MSOT at a $V_{B2} = 0$ cross section. The flux noise data (plot 11d) reveals both the blind spots (dark red) and also the fact that optimal sensitivity (dark blue) is found in only a small fraction of the fields (for a given constant V_{B2}). Both the blind spots and the optimal sensitivity points appear with intervals of $\sim \Phi_0/2$. In-situ shifting of the interference pattern is possible by changing V_{B2} and is demonstrated below. A close look at both interference patterns, the one at $V_{B1} > 0$, denoted I_c^+ and the other at $V_{B1} < 0$, denoted I_c^-, shows they are not centered around zero field (see inset to 11b): One is shifted to the right and the other to the left. There are two contributions for this asymmetry. The first is the 'circuit induced asymmetry' and the second is the 'intrinsic asymmetry', denoted ΔB_a^*. The intrinsic asymmetry is due to the junctions critical current asymmetry $a_i \neq a$ and inductance asymmetry $L_i \neq L/4$ of the SQUIDs branches [29].

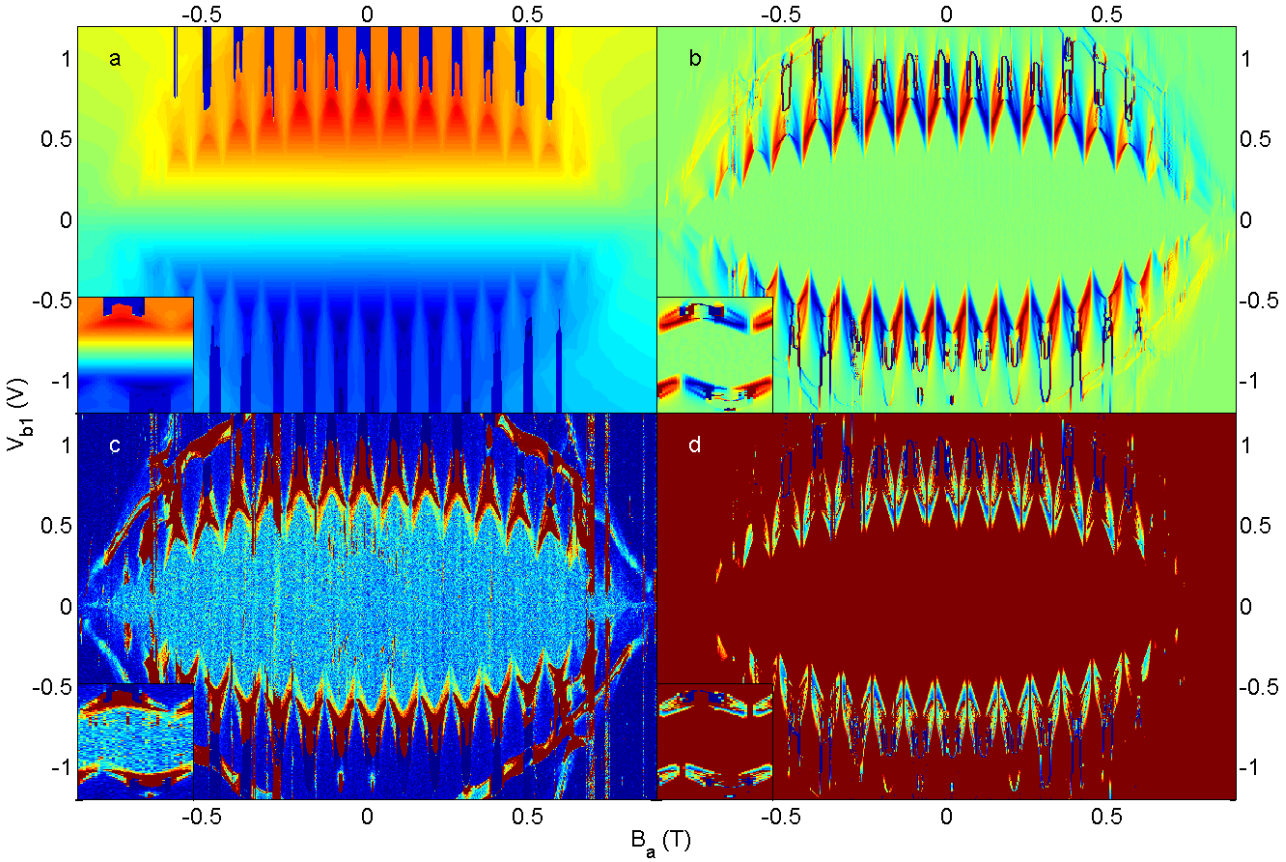

Figure 11: Interference patterns at $V_{B2} = 0$ cross section: (**a**) $V_{FB1} \in [-3,\ 3]$ V, (**b**)$dV_{FB1}/dB_a \in [-3,\ 3]$ mV/G, (**c**) $S_V|_{10\,\mathrm{kHz}} \in [400,\ 700]$ nV$/\sqrt{\mathrm{Hz}}$ and (**d**) $S_\Phi|_{10\,\mathrm{kHz}} \in [150,\ 500]$ n$\Phi_0/\sqrt{\mathrm{Hz}}$. The insets show a zoom in around $B_a = 0$, which make the asymmetry more apparent. The H_{c2} envelope suppresses SC completely at $B_a \approx 0.8\ T$. The inset of plot (d) reveals the blind spots for a given V_{B2} value.

Let us begin by explaining the circuit induced asymmetry. Assuming the MSOT is intrinsically symmetric, if we could set $I_2 = 0$ then both interference patterns would be symmetric around zero field because the MSOT becomes a right-left symmetric device. In our circuit, however, we do not

set I_2 but rather V_{B2}. This leaves I_2 dependent on V_{B1} (or I_1). Setting $V_{B2} = 0$ for example, the positive interference I_{c1}^{+} corresponds to $I_2 < 0$, shifting it to the left, towards lower fields. The negative interference I_{c1}^{-} is shifted to the right for a similar reason.

We now address the intrinsic asymmetry, ΔB_a^*. If we set $I_2 = 0$ (by setting for example a constant ratio of V_{B1}/V_{B2}) and the MSOT still shows asymmetry on the interference patterns, then it is due to intrinsic asymmetry of the device. In this case it is not right-left symmetric (even for $I_2 = 0$). To extract the intrinsic asymmetry from the measured data we therefore need to find the point of $I_{c1}^{max}|_{I_2=0}$ and ΔB_a^* is the field value at this point. This is how point (c) in Figure 8 is defined and it is found in the following manner. Up to this point I_c^{max} is constant and from this point on it starts reducing until it finally hits zero. We denote $V_{B2}^* \equiv V_{B2}|_{I_2=0}^{I_{c1}^{max}}$, see Figure 8. Its value is determined solely by the circuit's passive components using Kirchhoff's equations (section 5.2.1). This means that different intrinsic asymmetry values ΔB_a^* would only shift the I_{c1}^{max} curve horizontally and not vertically (at points (a) to (c), where I_{c1}^{max} is independent on V_{B2}).

Another observation could be made by considering time reversal symmetry. Applying it to the system corresponds to taking $V_{B1} \to -V_{B1}$, $V_{B2} \to -V_{B2}$ & $B_a \to -B_a$. The MSOT properties should be invariant under such a change. Figure (11) shows that this data indeed obeys this symmetry. The cross section is taken at $V_{B2} = 0$, thus under time reversal V_{B2} doesn't change and we are left with taking every point $\{B_a, V_{B1}\}$ symmetrically around the origin to its partner $\{-B_a, -V_{B1}\}$ in the opposite quadrant. This means that if the interference at $V_{B1} > 0$ is shifted to the right, then the interference at $V_{B1} < 0$ has to be shifted to the left by the same amount.

Figure 12 shows $I_{c1}(B_a, V_{B2})$ that was extracted from measured I-V curves. Changing V_{B2} shifts the interference pattern, allowing to position the optimal sensitivity points at the desired field thus eliminating the blind spots. Figure 12a shows that the interference pattern is shifted in a very simple manner, without changing its shape. This is in agreement with the analysis given in section 5.1.1. Figure 12a and b show that the two extreme values of V_{B2} shift the interference pattern by $\sim \Phi_0/2$. The circuit induced asymmetry allows an extra $\Phi_0/2$ shift by considering both $V_{B1} > 0$ and $V_{B1} < 0$ interference patterns giving a maximal total shift of Φ_0. Lastly, we note that the dark red regions in Figure 12 corresponds to the curve in Figure 8.

Comparing plot (b) and (c) of Figure 12 shows that for moderate values of V_{B2}, both interference patterns shift in the same direction upon changing V_{B2}, almost as a rigid body. This behavior is also in accordance with time reversal symmetry, which will be demonstrated below. As mentioned above, due to time reversal symmetry it is enough to measure only half of 3d space. Figure 12 shows data from exactly half of the space, in this case $B_a > 0$ out of which we reproduce the full space. The time reversed version of $I_{c1}^{-}(B_a > 0,\, V_{B2})$ is simply $I_{c1}^{+}(B_a < 0,\, -V_{B2})$. The full $I_{c1}^{+}(B_a \in [-0.9\,T,\, 0.9\,T])$ is found by taking plot (c) from Figure 12, mirror it around both X and Y axis and stitch it with plot (b) from the same Figure (Note that mirroring both X and Y is equivalent to rotating by 180 degrees). The result of this procedure is shown in Figure 13. To get the full I_{c1}^{-} we can simply rotate the last Figure by 180 degrees.

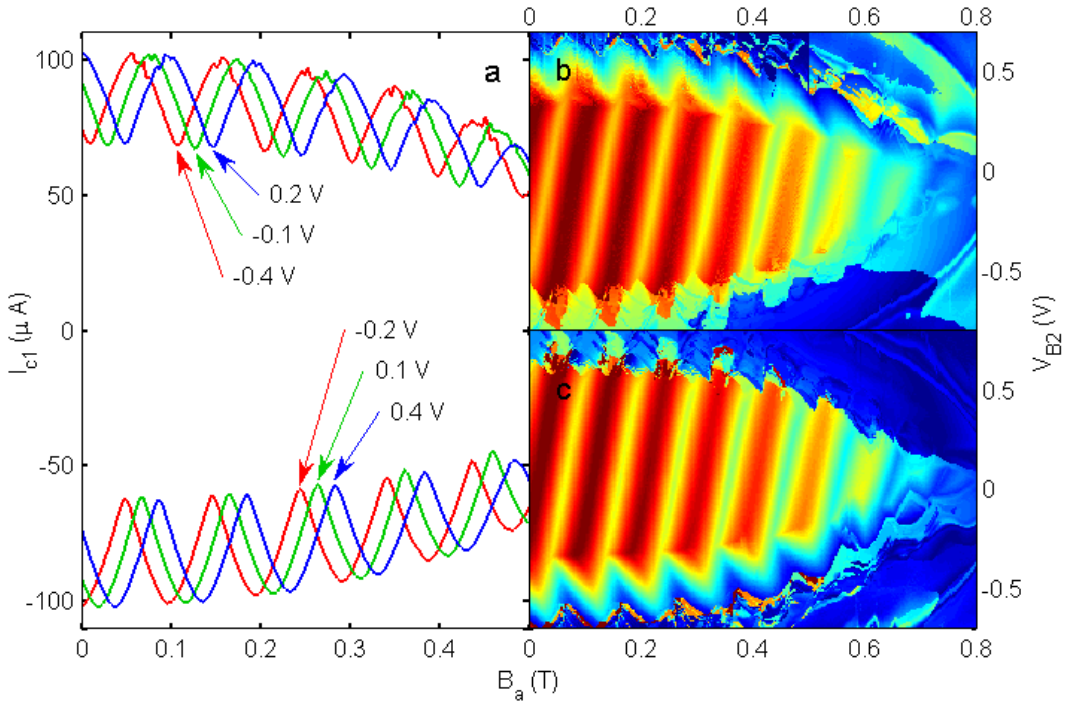

Figure 12: Critical current on terminal 1: (a) At selected V_{B2} values, showing both positive and negative critical currents, (b) Positive critical current I_{c1}^{+}, for continuous values of V_{B2}. The color range is from zero (blue) to 105 μA (red), (c) Same as (b) showing absolute value of negative critical current $\left|I_{c1}^{-}\right|$ with the same color range. The shifting of the interference pattern as function of V_{B2} is clearly illustrated.

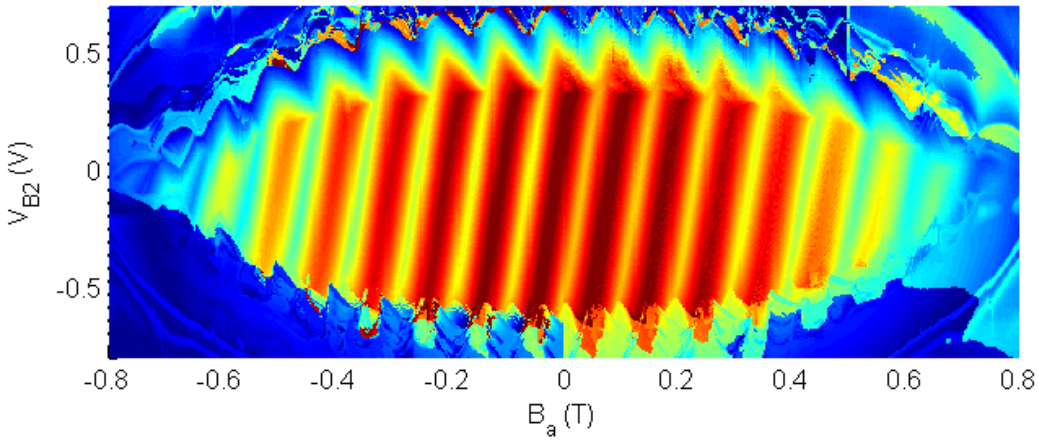

Figure 13: Reproduction of the full space from the $B_a > 0$ half of the space measured. Time reversed $I_{c1}^{-}(B_a > 0,\, V_{B2})$ is stitched with $I_{c1}^{+}(B_a > 0,\, V_{B2})$ which produces the full I_{c1}^{+} behavior.

A simulation of $I_{c1}^{+}(B_a, V_{B2})$ is presented in Figure 14. The main features of the DC regime are reproduced and understood (see section 5.2). Assuming sinusoidal CPR The maximal modulation

depth for a MSOT is achieved in the symmetric case $a_i = a$, $L_i = L/4$ and has a value of

$$\Delta I_c = \frac{I_c^{max} - I_c^{min}}{I_c^{max}} \approx 0.4,$$

Which is less than half compared with the optimal value of 1 for a conventional SQUID.

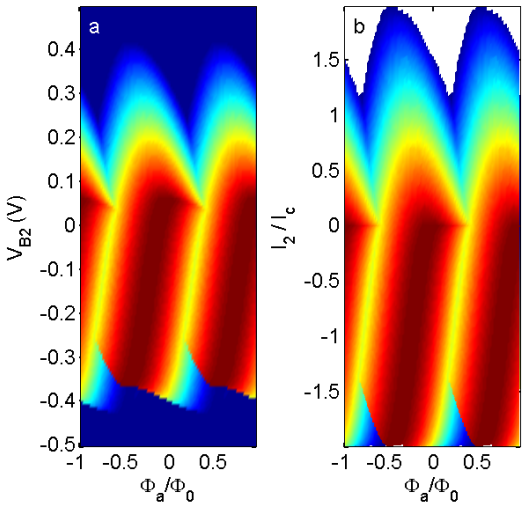

Figure 14: Simulation of (**a**) $I_{c1}^{+}/I_0\,(B_a, V_{B2})$ and (**b**) $I_{c1}^{+}/I_0\,(B_a, I_2)$. The color range is from 0 (blue) to 2 (red). The parameters used are $a_i = 1$, $I_0 = 50\,\mu$A, $L_i = 10/4$ pH, $R_{P,i} = 1\,\Omega$, $R_{S,i} = 5\,\Omega$, $R_{B1} = 5\,$kΩ and $R_{B2} = 3\,$kΩ.

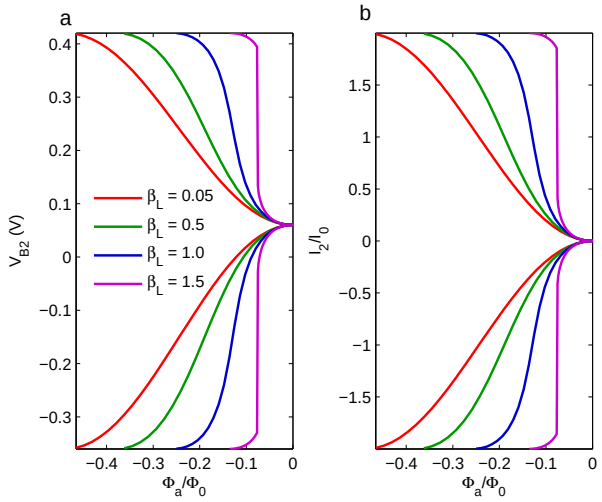

Figure 15: Simulation of (**a**) $I_{c1,max}^{+}\,(\Phi_a/\Phi_0, V_{B2})$ and (**b**) $I_{c1,max}^{+}\,(\Phi_a/\Phi_0, I_2/I_0)$ for different β_L values assuming sinusoidal CPRs. The parameters used are the same as in Figure 14, except L changes from 1 to 30 pH for $\beta_L = 0.05$ and 1.5 respectively. The maximal critical current for $V_{B2} = 0$ in plot (**a**) is shifted from $\Phi_a = 0$ to $\Phi_a/\Phi_0 \approx -0.1$ which is due to the circuit induced asymmetry. As expected, in plot (**b**) this shift is not apparent, since for $I_2 = 0$ the MSOT is left-right symmetric. For $\beta_L \ll 1$ the sinusoidal CPRs of junctions 1 and 2 are expressed in the shape of the curves.

To gain qualitative understanding on the influence of different parameters of the MSOT, L_i, a_i, etc. on the $I_c(\Phi_a, V_{B2})$ surface we plot only the maximal critical current curve $I_c^{max}(\Phi_a, V_{B2})$. This takes less calculation power and is done much faster. Decoupling the influence of the circuit is possible by considering the dependence of the critical current on I_2 rather than on V_{B2}, i.e. plotting $I_c^{max}(\Phi_a, I_2)$. An example of such a calculation, assuming sinusoidal CPRs is given in Figure 15.

A global view on the (beautiful) 3d parameter space of the MSOT is given in Figure 16, showing the MSOT's response dV_{FB1}/dB_a. The shift of the $I_c(\Phi)$ interference pattern is made clear by comparing both $V_{B2} = const.$ cross sections. The $V_{B1} = const.$ cross section shows the shift at the voltage state. It follows similar lines to those of the $I_c(\Phi)$ pattern. Lastly, the $B_a = const.$ cross section is important from a practical point of view. Using the MSOT as a magnetometer, given the average magnetic field to be measured, we can use this cross section to find the WP, i.e. the pair $\{V_{B1}, V_{B2}\}$ that gives the best sensitivity.

With this practical consideration in mind, we now set out to find the best WP for every given field. This is done using a computer algorithm that considers both best sensitivity and also avoids WPs that have very small volume in the 3d space below some noise threshold. The 3d data was taken with field intervals of 30 G, so that we can find a different WP every 30 G. The result of this procedure is presented in Figure 17 for a few selected field values with a total range that corresponds to $\sim \Phi_0$.

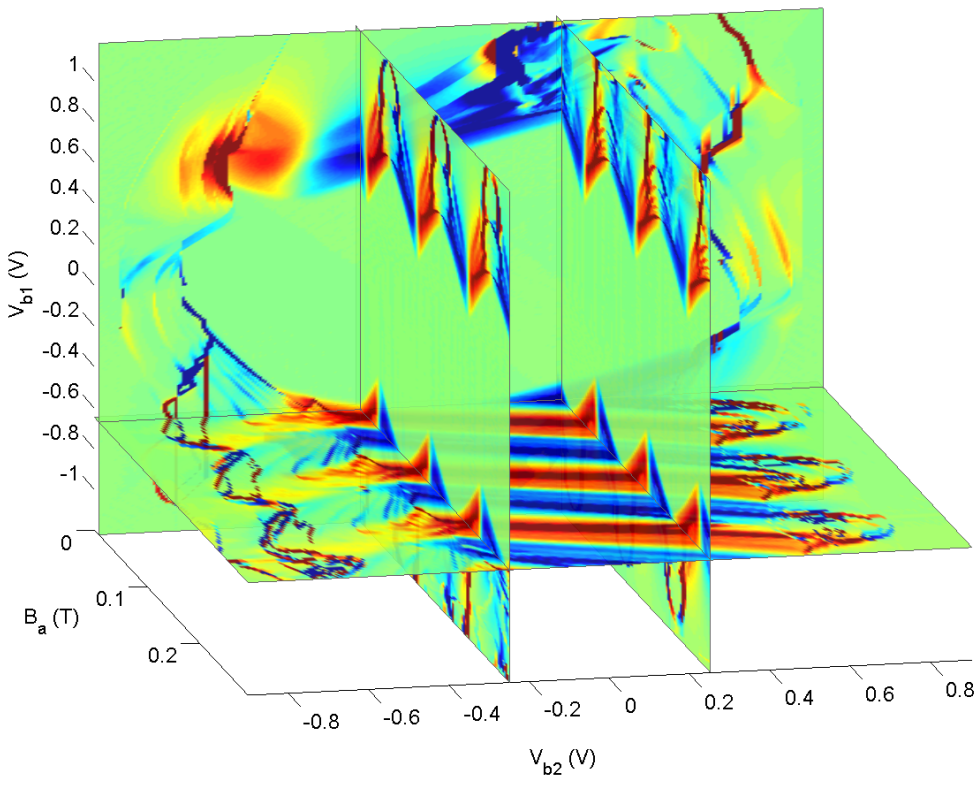

Figure 16: MSOT response in the 3d parameter space: $dV_{FB1}/dB_a(V_{B1}, V_{B2}, B_a)$. The color range is from -3 (blue) to 3 mV/G (red). The shift of the interference pattern in the voltage state is clearly demonstrated by comparing both $V_{B2} = const.$ cross sections.

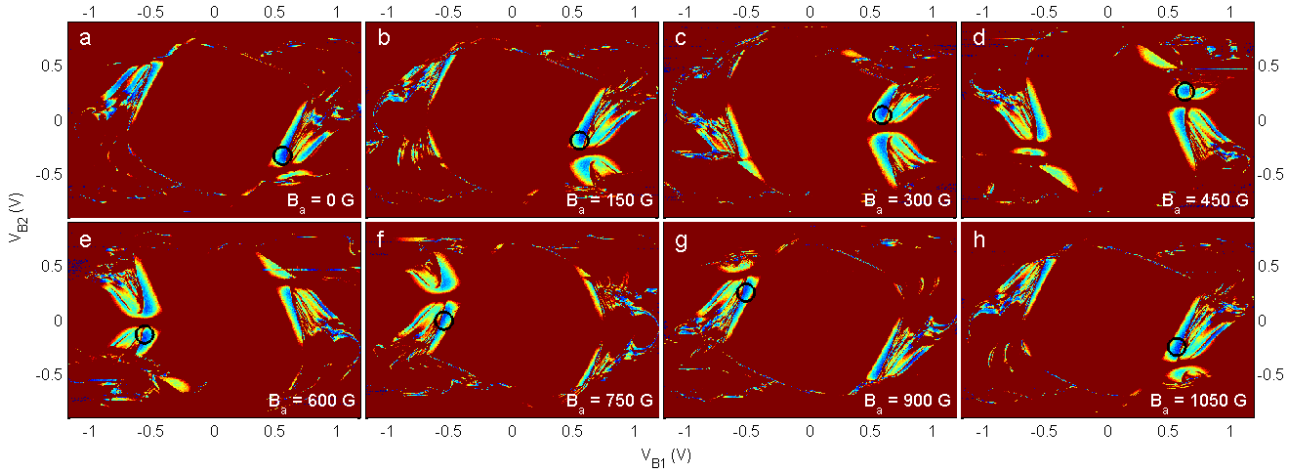

Figure 17: Flux noise as a function of the bias voltages at different constant fields, corresponding to a total range of $\sim \Phi_0$. The color range is from 150 (blue) to 500 $\mathrm{n}\Phi_0/\sqrt{Hz}$ (red). For every field value a black circle indicates the point with minimal noise found by the computer algorithm. These so called 'working points' are pairs of $\{V_{B1}, V_{B2}\}(B_a)$ creating a 1d trajectory in the 3d parameter space. The spectrum analyzer noise measurement is then performed on this trajectory.

6.3 Noise measurements on the 1d trajectory

The set of WPs $\{V_{B1}, V_{B2}\}(B_a)$ is now used to take noise measurements with a spectrum analyzer. The basic principle is to set B_a, then set V_{B1} and V_{B2} at which the flux noise is lowest and measure V_{FB} at both DC and the spectra. The field intervals were 3 G, i.e. a density 10 times higher compared to the 3d data measurement. One can therefore change WP every 10 points. The higher density is due to two reasons. First, since it is a 1d trajectory the measurement is in general much shorter and we can afford taking more points compared to the 3d space measurement. Second, whenever we change the WP, we cannot calculate the response dV_{FB}/B_a. It is simply meaningless. To avoid this problem we let the measurement run three times, changing WP every 90 G in shifted field values. That is, on the first measurement the WP was changed at $B_a = 0$ G, 90 G, ..., on the second at $B_a = 30$ G, 120 G, ... and on the third at $B_a = 60$ G, 150 G, ... The spectrum analyzer was set to measure power spectral density (PSD) root mean square (RMS) voltage noise on the V_{FB} signal. The three measurements took a total of 6 hours. The response was calculated numerically from the DC data, using a symmetric derivative:

$$\frac{dV_{FB}}{dB_a}|_{B_{a,0}} = \frac{V_{FB}(B_{a,0} + \Delta B_a) - V_{FB}(B_{a,0} - \Delta B_a)}{2\Delta B_a},$$

Where $\Delta B_a = 3$ G. The flux noise in units of $\Phi_0/\sqrt{\mathrm{Hz}}$ was calculated according to:

$$\sqrt{S_\Phi} = \frac{\sqrt{S_V} A_{eff}}{|dV_{FB}/dB_a|\,\Phi_0},$$

where $A_{eff} \equiv \Phi_0/B_a^0$ is the effective area of the MSOT calculated from it's magnetic field period B_a^0. The spin noise, assuming the dipole is in the center of the MSOT's ring is calculated using equation 1. Figure 18 shows the spectrum at $B_a = 0.2$ T. It shows $1/f$ noise up to ~ 1 kHz and white noise above it. At 30 kHz the spectra is rather flat and represents the noise from 1 kHz to 100 kHz excluding three peaks at 40, 60 & 80 kHz. This spectrum qualitatively represents the spectra at all fields up to H_{c2}.

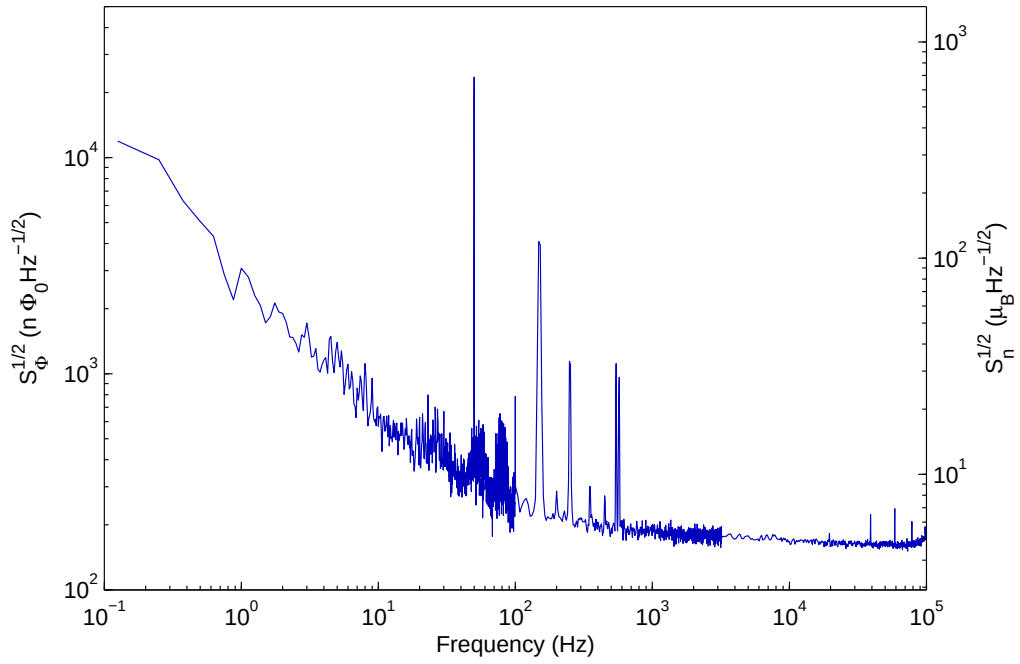

Figure 18: Spectrum, for B_a = 0.2 T at the optimal WP, shown in dimensions of flux noise (left axis) as well as spin noise (right axis). Below 1 kHz $1/f$ noise is apparent and above this frequency there is white noise of ~200 n$\Phi_0/\sqrt{\text{Hz}}$ and 5 $\mu_B/\sqrt{\text{Hz}}$.

Figure 19 shows the average noise at 30 ± 5 kHz for fields ranging from 0 to H_{c2}. This data represents the strong point of the MSOT, namely - high, nearly constant sensitivity at *continuous* fields up to H_{c2}, including zero field.

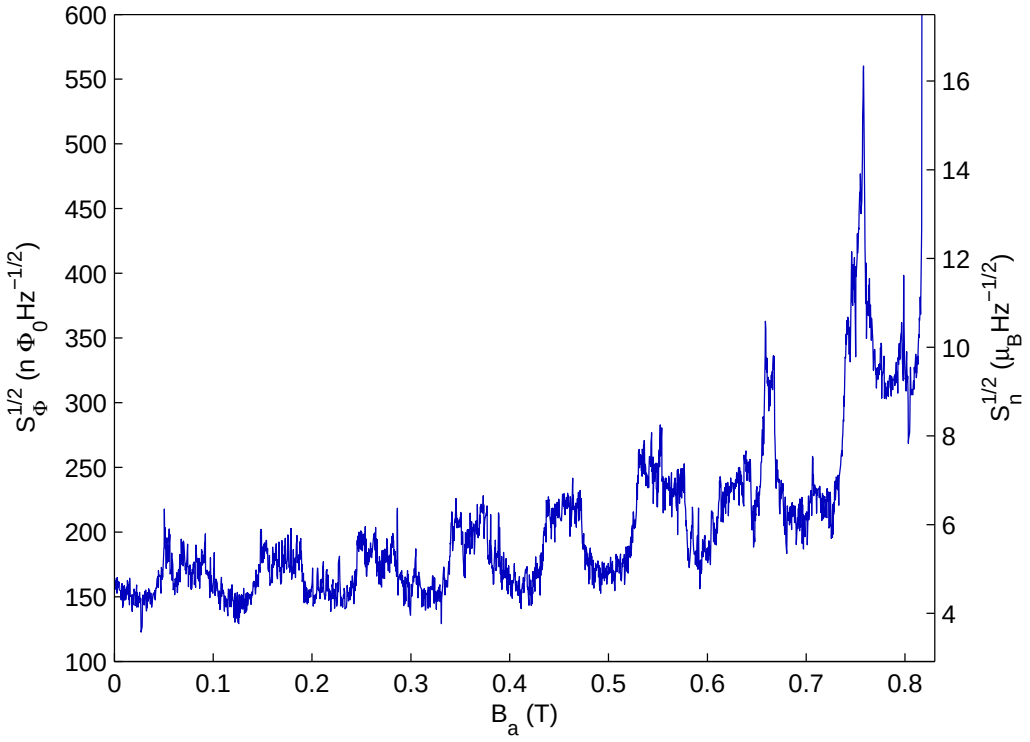

Figure 19: MSOT noise at 30 kHz shown in dimensions of flux noise (left axis) as well as spin noise (right axis). The noise measurements were taken at the optimal WP for each field value. The MSOT shows noise levels of less than 370 $n\Phi_0/\sqrt{\text{Hz}}$ in flux noise which corresponds to 11 $\mu_B/\sqrt{\text{Hz}}$ in spin noise and 34 $\text{nT}/\sqrt{\text{Hz}}$ in magnetic field noise for continuous field values ranging from 0 to 0.75 T, which is very close to $H_{c2} \approx 0.8$T. At the majority of the fields the noise levels are as low as 200 $n\Phi_0/\sqrt{\text{Hz}}$, 6 $\mu_B/\sqrt{\text{Hz}}$ and 20 $\text{nT}/\sqrt{\text{Hz}}$.

7 Summary

A novel four-terminal, four-junction 165 nm diameter Pb MSOT was fabricated and characterized for the first time. The device shows low noise levels, which are comparable to our two junction two terminal SOTs. The in-situ control over the $I_c(\Phi_a)$ interference pattern eliminates the blind spots resulting in low noise for continuous fields from zero up to H_{c2}. Further progress can be made by reducing the device diameter. A MSOT with a diameter of 120 nm was already successfully fabricated and we believe a sub 100 nm diameter is also feasible. This should improve spin noise, setting the goal at $S_n^{1/2} \lesssim 1\ \mu_B/\sqrt{\text{Hz}}$ and might also increase the field dynamic range by increasing H_{c2}. In terms of modulation depth it seems that we are already close to the optimal value of ~ 0.4. The most important milestone for the MSOT, however is its incorporation in the liquid ^{4}He scanning microscope to probe physics that was not accessible to us in the past.

References

[1] D. Vasyukov, Y. Anahory, L. Embon, D. Halbertal, J. Cuppens, L. Neeman, A. Finkler, Y. Segev, Y. Myasoedov, M. L. Rappaport, M. E. Huber, and E. Zeldov, "A scanning superconducting quantum interference device with single electron spin sensitivity." *Nature nanotechnology*, vol. 8, no. September, pp. 639–44, 2013. [Online]. Available: http://www.ncbi.nlm.nih.gov/pubmed/23995454

[2] M. S. Grinolds, S. Hong, P. Maletinsky, L. Luan, M. D. Lukin, R. L. Walsworth, and A. Yacoby, "Nanoscale magnetic imaging of a single electron spin under ambient conditions," *Nat Phys*, vol. 9, no. 4, pp. 215–219, Feb 2013. [Online]. Available: http://dx.doi.org/10.1038/nphys2543

[3] C. Degen, "Nanoscale magnetometry: Microscopy with single spins," *Nature Nanotechnology*, vol. 3, no. 11, pp. 643–644, Nov 2008. [Online]. Available: http://dx.doi.org/10.1038/nnano.2008.328

[4] D. Rugar, R. Budakian, H. J. Mamin, and B. W. Chui, "Single spin detection by magnetic resonance force microscopy," *Nature*, vol. 430, no. 6997, pp. 329–332, Jul 2004. [Online]. Available: http://dx.doi.org/10.1038/nature02658

[5] J. R. Maze, P. L. Stanwix, J. S. Hodges, S. Hong, J. M. Taylor, P. Cappellaro, L. Jiang, M. V. G. Dutt, E. Togan, A. S. Zibrov, and et al., "Nanoscale magnetic sensing with an individual electronic spin in diamond," *Nature*, vol. 455, no. 7213, pp. 644–647, Oct 2008. [Online]. Available: http://dx.doi.org/10.1038/nature07279

[6] G. Balasubramanian, I. Y. Chan, R. Kolesov, M. Al-Hmoud, J. Tisler, C. Shin, C. Kim, A. Wojcik, P. R. Hemmer, A. Krueger, and et al., "Nanoscale imaging magnetometry with diamond spins under ambient conditions," *Nature*, vol. 455, no. 7213, pp. 648–651, Oct 2008. [Online]. Available: http://dx.doi.org/10.1038/nature07278

[7] P. Maletinsky, S. Hong, M. S. Grinolds, B. Hausmann, M. D. Lukin, R. L. Walsworth, M. Loncar, and A. Yacoby, "A robust scanning diamond sensor for nanoscale imaging with single nitrogen-vacancy centres," *Nature Nanotechnology*, vol. 7, no. 5, pp. 320–324, Apr 2012. [Online]. Available: http://dx.doi.org/10.1038/nnano.2012.50

[8] G. Boero, M. Demierre, P.-A. Besse, and R. Popovic, "Micro-hall devices: performance, technologies and applications," *Sensors and Actuators A: Physical*, vol. 106, no. 1-3, pp. 314–320, Sep 2003. [Online]. Available: http://dx.doi.org/10.1016/S0924-4247(03)00192-4

[9] N. C. Koshnick, M. E. Huber, J. A. Bert, C. W. Hicks, J. Large, H. Edwards, and K. A. Moler, "A terraced scanning supper conducting quantum interference device susceptometer with submicron pickup loops," *Applied Physics Letters*, vol. 93, pp. 6–9, 2008.

[10] M. E. Huber, N. C. Koshnick, H. Bluhm, L. J. Archuleta, T. Azua, P. G. Bjornsson, B. W. Gardner, S. T. Halloran, E. A. Lucero, and K. A. Moler, "Gradiometric micro-squid susceptometer for scanning measurements of mesoscopic samples," *Review of Scientific Instruments*, vol. 79, no. 5, p. 053704, 2008. [Online]. Available: http://dx.doi.org/10.1063/1.2932341

[11] M. B. Ketchen, D. D. Awschalom, W. J. Gallagher, A. W. Kleinsasser, R. L. Sandstrom, J. R. Rozen, and B. Bumble, "Design, fabrication, and performance of integrated miniature squid susceptometers," *IEEE Transactions on Magnetics*, vol. 25, no. 2, pp. 1212–1215, 1989.

[12] A. Finkler, Y. Segev, Y. Myasoedov, M. L. Rappaport, L. Ne'Eman, D. Vasyukov, E. Zeldov, M. E. Huber, J. Martin, and A. Yacoby, "Self-aligned nanoscale squid on a tip," *Nano Letters*, vol. 10, pp. 1046–1049, 2010.

[13] A. Finkler, D. Vasyukov, Y. Segev, L. Neeman, E. O. Lachman, M. L. Rappaport, Y. Myasoedov, E. Zeldov, and M. E. Huber, "Scanning superconducting quantum interference device on a tip for magnetic imaging of nanoscale phenomena," *Review of Scientific Instruments*, vol. 83, 2012.

[14] A. Finkler, D. Vasyukov, Y. Segev, L. Neeman, Y. Anahory, Y. Myasoedov, M. L. Rappaport, M. E. Huber, J. Martin, a. Yacoby, and E. Zeldov, "Nano-sized squid-on-tip for scanning probe microscopy," *Journal of Physics: Conference Series*, vol. 400, p. 052004, 2012. [Online]. Available: http://iopscience.iop.org/1742-6596/400/5/052004

[15] Y. Anahory, J. Reiner, L. Embon, D. Halbertal, A. Yakovenko, Y. Myasoedov, M. L. Rappaport, M. E. Huber, and E. Zeldov, "Three-junction squid-on-tip with tunable in-plane and out-of-plane magnetic field sensitivity," *Nano Lett.*, vol. 14, no. 11, pp. 6481–6487, Nov 2014. [Online]. Available: http://dx.doi.org/10.1021/nl503022q

[16] L. Embon, Y. Anahory, A. Suhov, D. Halbertal, J. Cuppens, A. Yakovenko, A. Uri, Y. Myasoedov, M. L. Rappaport, M. E. Huber, A. Gurevich, and E. Zeldov, "Probing dynamics and pinning of single vortices in superconductors at nanometer scales," *Sci. Rep.*, vol. 5, pp. –, Jan. 2015. [Online]. Available: http://dx.doi.org/10.1038/srep07598

[17] M. Tinkham, *Introduction to Superconductivity*, 2nd ed. McGraw-Hill, 1996.

[18] L. N. Cooper, "Bound electron pairs in a degenerate fermi gas," *Physical Review*, vol. 104, no. 4, pp. 1189–1190, 1956.

[19] K. Onnes, "Further experiments with liquid helium," *Leiden Communications*, vol. 120b, pp. 1479–1481, 1911.

[20] W. Meissner and R. Ochsenfeld, "Ein neuer effekt bei eintritt der supraleitfhigkeit," *Die Naturwissenschaften*, vol. 21, no. 44, pp. 787–788, Nov 1933. [Online]. Available: http://dx.doi.org/10.1007/BF01504252

[21] J. Bardeen, L. N. Cooper, and J. R. Schrieffer, "Theory of superconductivity," *Phys. Rev.*, vol. 108, pp. 1175–1204, Dec 1957. [Online]. Available: http://link.aps.org/doi/10.1103/PhysRev.108.1175

[22] V. Ginzburg and L. Landau, *Zh. Eksp. Teor. Fiz.*, vol. 20, p. 1064, 1950.

[23] L. Gor'kov, "Microscopic derivation of the ginzburg-landau equations in the theory of superconductivity," *Soviet Physics JETP*, vol. 36, no. 6, pp. 1364–1367, 1959. [Online]. Available: http://www.w2agz.com/Library/Classic Papers in Superconductivity\npapers2://publication/uuid/72839D12-27FF-4665-BB37-0C436BEAE56A

[24] L. Onsager, "Magnetic flux through a superconducting ring," *Physical Review Letters*, vol. 7, no. 2, p. 50, 1961.

[25] A. A. Abrikosov, "On the magnetic properties of superconductors of the second group," *Sov-Phys JETP*, vol. 5, pp. 1174–1182, 1957.

[26] B. Josephson, "Possible new effects in superconductive tunnelling," *Physics Letters*, vol. 1, no. July, pp. 251–253, 1962.

[27] K. K. Likharev, "Superconducting weak links," *Reviews of Modern Physics*, vol. 51, no. 1, pp. 101–159, 1979.

[28] J. C. and A.I.Braginski, *The SQUID Handbook: Vol. 1 Fundamental and technology of SQUIDs and SQUIDs Systems*, J. Clarke and A.I.Braginski, Eds. Wiley-VCH, 2004.

[29] C. D. Tesche and J. Clarke, "dc squid: Noise and optimization," *Journal of Low Temperature Physics*, vol. 29, pp. 301–331, 1977.

[30] K. Hasselbach, D. Mailly, and J. R. Kirtley, "Micro-superconducting quantum interference device characteristics," *Journal of Applied Physics*, vol. 91, no. 2002, pp. 4432–4437, 2002.

[31] T. V. Duzer and W. T. Tsang, "Influence of the current-phase relation on the critical-current-applied-magnetic-flux dependence in parrallel-connected josephson junctions," *J. Appl. Phys.*, vol. 47, pp. 2656–2661, 1976.

[32] M. E. Huber, P. a. Neil, R. G. Benson, D. a. Burns, A. M. Corey, C. S. Flynn, Y. Kitaygorodskaya, O. Massihzadeh, J. M. Martinis, and G. C. Hilton, "Dc squid series array amplifiers with 120 mhz bandwidth," *IEEE Transactions on Applied Superconductivity*, vol. 11, pp. 1251–1256, 2001.

[33] E. Yaakobi, "Squid-on-tip characterization and improvement using integrated resistive shunt-on-tip," Master's thesis, WIS, 2014.

[34] D. S. G. David A. Cardwell, *Handbook of Superconducting Materials*. CRC Press, 2002.

8 Appendices

8.1 MSOT parameters extraction

As a multi-terminal multi-junction device, the MSOT has many parameters determining its behavior. It also has many observables that in principle might allow to extract the parameters by fitting a simulation to the measured data. This procedure is yet to be mastered. In spite of this we present here a rough preliminary estimate to a few important parameters.

Estimating ξ for the SQUID's ring can be done by using the relation $H_{c2}(T) = \frac{\Phi_0}{2\pi\xi(T)^2}$ [28]. For the measured $H_{c2}(T = 4.2\text{ K}) \approx 0.8$ T, the coherence length is

$$\xi(4.2\text{ K}) \approx 20\text{ nm}.$$

The Dayem bridges width w and length L can be estimated from the SEM image to be $w = 25 \pm 5$ nm and $L = 30 \pm 10$ nm (see Figure 20) and the thickness t can be roughly estimated by the deposition thickness $t \approx 12$ nm. The junction length L is thus of order ξ. This should give sinusoidal CPRs and optimal $I_c(\Phi_a)$ dependence.

The modulation depths for the positive and negative I_c curves around $B_a = 0$ are $\Delta I_c^+ = 0.34 \pm 0.01$ and $\Delta I_c^- = 0.40 \pm 0.01$. The difference between the two values is yet to be explained. Defining the skewness of the $I_c(\Phi_a)$ curves as

$$S \equiv \frac{\Delta B_{a,1} - \Delta B_{a,2}}{\Delta B_{a,1} + \Delta B_{a,2}},$$

where $\Delta B_{a,1} = B_a|_{I_c^{min}} - B_a|_{I_c^{max1}}$, $\Delta B_{a,2} = B_a|_{I_c^{max2}} - B_a|_{I_c^{min}}$ and we consider two neighboring maxima of the I_c curve, max_1 and max_2. With this definition $S \in [-1, 1]$. The measured MSOT gives $S^+ = -0.06 \pm 0.03$ and $S^- = 0.03 \pm 0.03$ for the positive and negative $I_{c1}(\Phi)$ curves respectively. The total inductance L can be estimated by comparing the modulation depth and the skewness to simulations. We estimate $L = 1^{+9}_{-1}$ pH. As mentioned above, the kinetic inductance of our devices dominates the geometric inductance so that $L \approx L_k$. The London penetration depth λ_L can be estimated by using $L_k = 2\pi\mu_0\lambda_L^2 R/a$ [34], where $R = 165/2$ nm is the loop radius and $a \approx 12 \times 25$ nm^2 is the estimated cross section of the loop. This gives $\lambda_L = \sqrt{\frac{aL_k}{2\pi\mu_0 R}} = 20^{+50}_{-20}$ nm, comparable to the bulk Pb penetration depth $\lambda_L = 37$ nm [28]. We thus find that the junctions' dimensions are comparable to both λ and ξ. The Ginzburg Landau parameter is $\kappa \equiv \lambda_L/\xi = 1^{+2.5}_{-1} \lesssim 1/\sqrt{2}$, which corresponds to borderline type II superconductor.

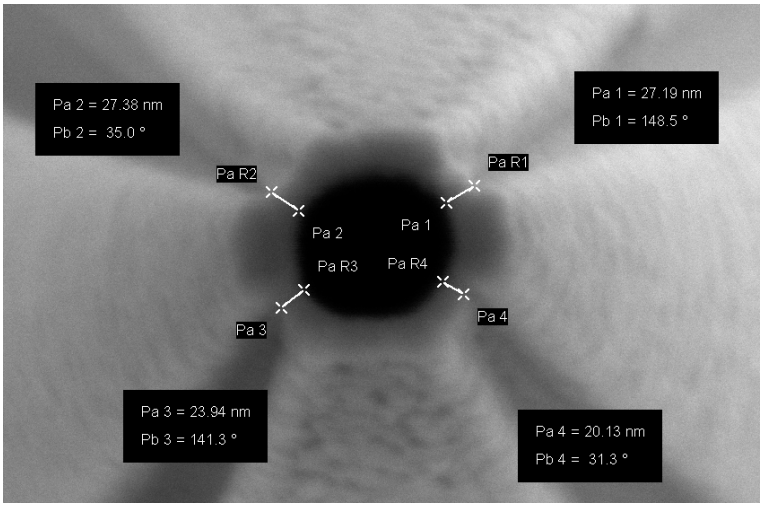

Figure 20: SEM image showing the dimensions of the Dayem bridges.

8.2 Pulling parameters, tube material and design

Table 1 and Figure 21 shows different pulling parameters and the resulting tip diameter. The tip's effective diameter determined by its interference pattern will usually be ~10% smaller than the outer diameter of the bare tip, prior to deposition which can be measured by a SEM. Figure 21 shows both values for two different tips. The number of tips presented is small because only not many tips were fabricated with the current MSOT quartz tubes design. However, the linear dependency of the tip's diameter on the hard pull parameter at moderate hard pull values (70 to ~120) is well established from the work with other quartz tubes in the lab. Using the pulling parameters given in table 1 there seems to be an upper limit on the tip's diameter around $\sim$ 200 nm. Reducing the hard pull parameter to values of 65 and below, the tip tend to break with unpredictable diameter, ranging from 1 to 10 μm with a rough and unusable apex surface. To get tips of diameters larger than ~200 nm different pulling parameters should be used.

Attempts of using borosilicate instead of quartz shows that borosilicate is inferior. First, it is more brittle and requires handling with much more care. Second, when imaging a bare borosilicate tip in the SEM it tends to deform. Lastly, it seems that the required pulling parameters are determined mainly by the tube's material and are almost indifferent to its shape. That is, quartz tubes of different shapes can be pulled with the same pulling parameters to achieve almost the same result, whereas for borosilicate tubes one needs to use a different set of parameters altogether.

Heat	Filament	Velocity	Delay	Hard pull
800	5	20	128	118
650	4	75	128	x

Table 1: MSOT pulling parameters for Sutter Instruments P-2000 puller. The hard pull parameter x ranges from ~65 for large diameter tips to ~100 for smaller ones.

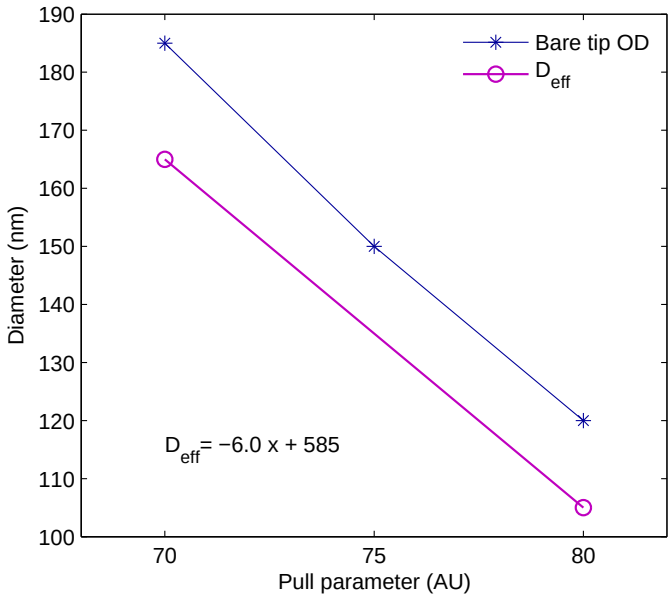

Figure 21: The tip diameter's dependence on the hard pull parameters, denoted x in table 1. Higher hard pull value results in a smaller tip diameter. The tip's effective diameter, determined by its interference pattern, is usually ~10% less than the outer diameter of the bare tip's apex.

8.2.1 MSOT quartz tube design

Figure 22 shows the design of the MSOT quartz tubes according to which the tubes were fabricated by the company F&D.

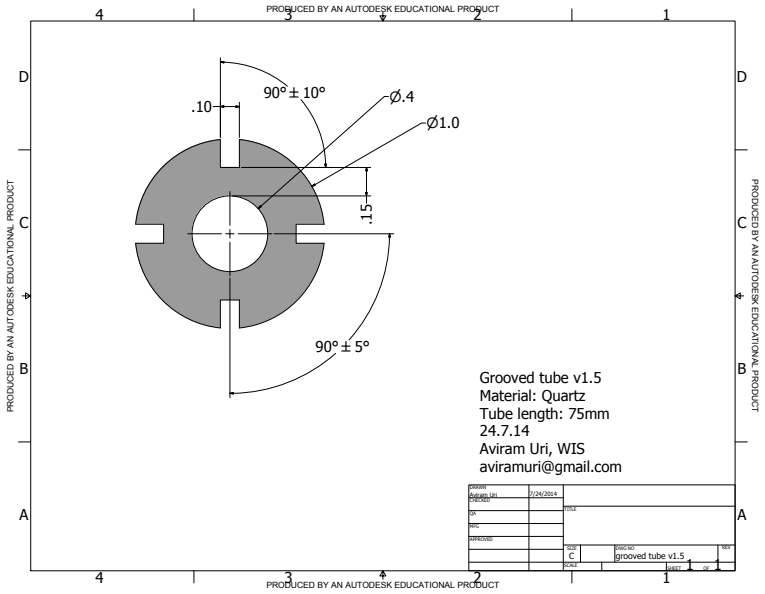

Figure 22: MSOT quartz tube design. The tubes were fabricated by the company F&D.

8.3 Deposition considerations

Figure 23 shows two tips that were deposited using relatively low exchange gas pressure of 5×10^{-6} Torr resulting in bad adhesion and an unusable tip. The more conventional two terminals and two junctions SOTs, so called, 'O-tips', fabricated in the lab are usually cooled down with this low exchange gas pressure and show good adhesion. The reason for this is as follows. The mechanical assembly holding the tip and electrically connecting it to the measurement system is called a tip holder. The O-tips' tip holder provides good thermal contact of the Au leads with the cryostat via metallic parts only. The tip, it seems, is cooled down mainly due to this good thermal anchoring and there is little need for the exchange gas cooling. In the case of the MSOT however, the assembly is different (Figure 25) and involves also plastic (PEEK) parts which make the thermal contact of the tip and the cryostat very poor. This must be compensated with high pressure exchange gas of $\sim 5 \times 10^{-3}$ Torr.

The orientation of the MSOT in the tip holder is also of key importance. It is oriented such that the depositions are directed on leads 1 and 3, rather than on the grooves. Positioning the tip by eye allows for about ± 5 degrees accuracy which is accurate enough. A larger orientation mistake would result in the absence of one of the junctions (see for example the right tip in Figure 23). As mentioned in the main text, the Au and Pb deposition must be done in in the same direction to prevent the Au from shorting two adjacent Pb leads.

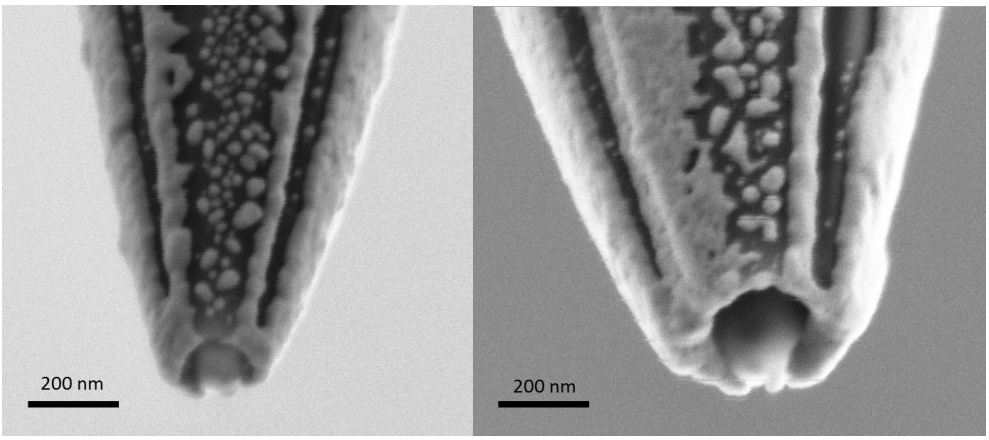

Figure 23: SEM images showing bad adhesion quality of the Pb to the Quartz in two different MSOT tips (left to right: tip 140717_1 and tip 140807_1). This is due to poor cooling of the tip prior to deposition. In both cases low pressure ^{4}He exchange gas of 5×10^{-6} Torr was used. The ring was clearly not formed. On the right image the tip was also not oriented accurately enough resulting in the absence of the left junction seen in the image. The left and middle leads are effectively shorted together without a weak link between them.

8.4 System Design

Figures 24 and 25 show photographs of the tip holder and of the cold side of the probe.

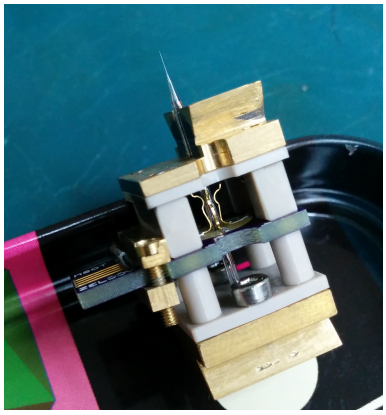

Figure 24: Photograph of the tip holder. Visible from top to bottom: The tip, three of the four spring electrical contacts and the tip holder PCB. The light gray parts are made out of PEEK plastic to avoid electrical shorting of the four contacts.

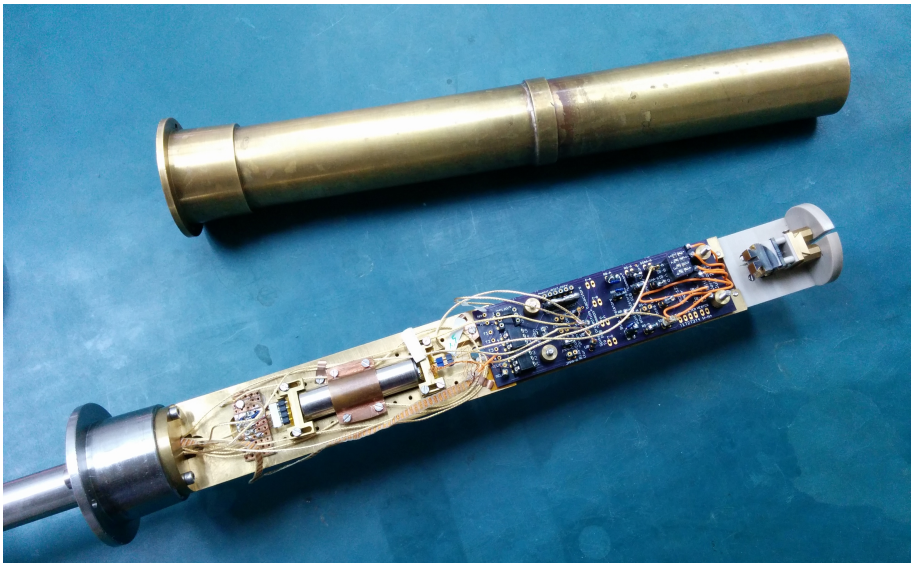

Figure 25: Photograph of the cold side of the probe. Visible from right to left: the tip holder, the probe PCB, one of the SSAAs' shields. At the top of the photo is the vacuum can.

8.4.1 Printed circuit board (PCB) design

The electrical circuit was realized using a printed circuit board (PCB). The connectivity scheme of the PCB is shown in Figure 26 and its physical realization in Figures 27 and 28. Biasing of the MSOT is done by four coax wires going from the room temperature side down to the PCB, connecting to it on the points denoted 'VB-A' to 'VB-D'. The outer shield of these coaxes is connected to the probe's body. The bottom left mount drill is plated in order to electrically short it to the probe's body via

the screw and nut holding the PCB in place. The plating is connected to a jumper, denoted 'JMPR' that allows connecting (or floating) the ground plane of the PCB, denoted 'GND', to the probe's body. Usually one of the MSOT's terminals is used as a drain, i.e. is not biased but grounded. In the experiment presented in this work it was terminal 3 of the MSOT. The docks 'JMPR-A' to 'JMPR-D' are used for this purpose. Observing the schematics following one of the terminals, say terminal A, starting from the bias point 'VB-A' and progressing to the right we find the following elements. 'C-A' dock allows mounting a surface mount capacitor shunt to ground that would act as a low pass filter on the bias line. In the current setup it was not in use since the low pass filter was at the room temperature side of the bias line. The 'RB-A' dock is used for the bias resistor R_{B1} and the 'RS-A' dock for the shunt resistor R_{S1}. The 'SSAA-A' dock allows connecting one of the two SSAAs to measure the current on terminal A. For all the terminals that are not floating and current isn't being measured upon one should short this dock with a jumper to allow current flow through the terminal. 'IB-A' to 'IB-D' denotes the current biased points. From these points different connectivity can be used. The notation A, B, C & D is used for the room temperature biases, while the notation 1, 2, 3 & 4 is used to denote the MSOT terminals. The two sets can be connected in all possible configurations (for example: A-1, B-2, C-3 & D-4, or A-2, B-1, C-4, D-3). This is done using a small ~10X10 mm^2 PCB that connects ports 'IB-A' - 'IB-D' with ports 'IB1' - 'IB4' (see Figure 28). Finally the 'IB-1' point is connected to the MSOT tip holder via a wire and a commercial socket that allows snap in connection of the tip holder to the probe. Ports 5 and 6 are reminiscent of an older design of the MSOT, the so called 'Triple Barrel' quartz tubes, that involved 6 terminals and are currently not in use. Two optical relays are used to short all the MSOT's terminals together to protect is from current spikes in the preparation stage. The third relay is not in use (also a reminiscent of the six contact tips). The relays used are Vishay VO14642 normally open solid state PCB mount relays. Subjected to 20 mA on contacts 1 and 3 (the positive bias on contact 1) they short together contacts 4, 5 & 6. The 'Mechanical-Short-i', 'Magic-Box-i' and the optical relay i ports are shorted together and are also shorted to the tip bias point 'IB-i'. They allow testing the MSOT's room temperature resistance prior to cooling it down to make sure it is not an open circuit. One can test each MSOT terminal separately by shorting all but one of the four terminals and measuring the resistance of this terminal to all the rest.

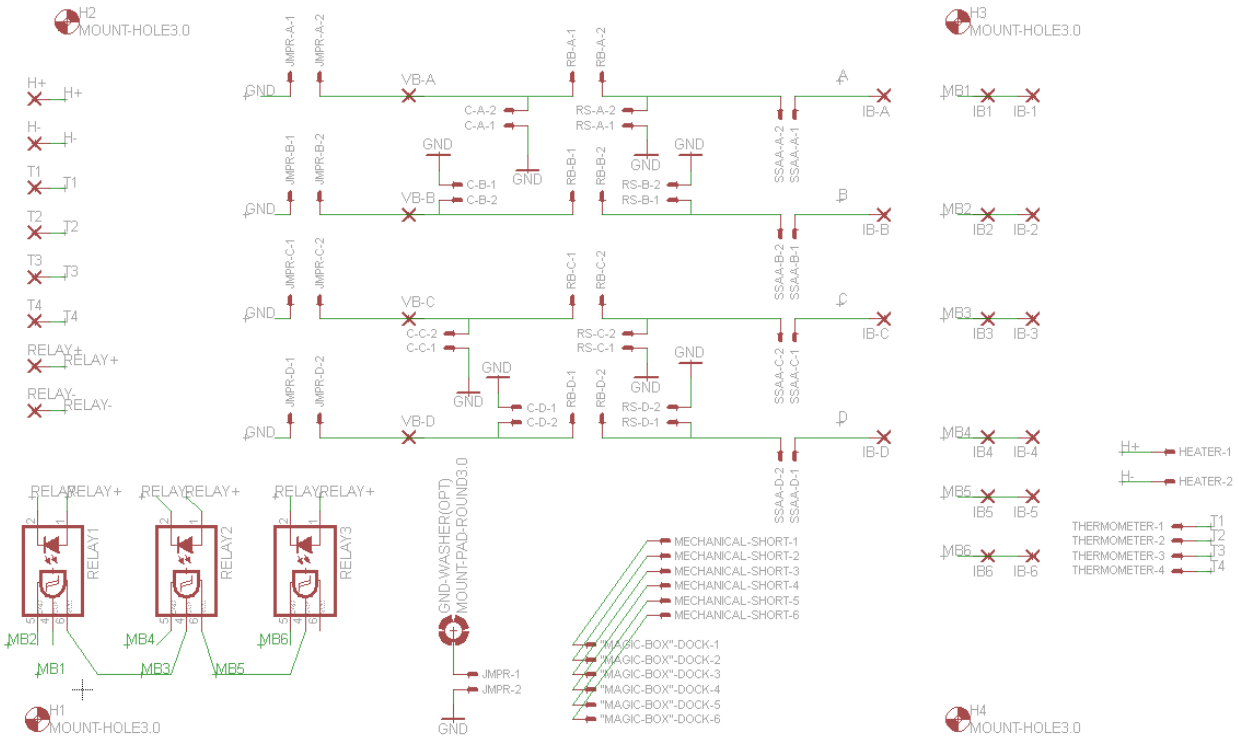

Figure 26: Connectivity scheme of the PCB used in the MSOT setup. The design allows connectivity flexibility.

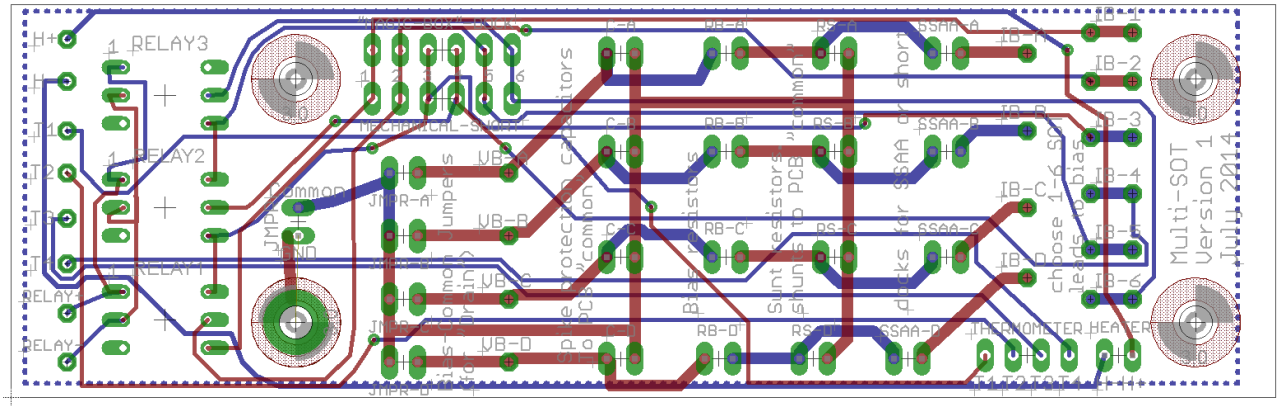

Figure 27: The PCB layout showing top copper layer (red), bottom copper layer (blue), pads and plated through (via) holes (green), silkscreen (gray) and the four mounting drills (dotted red/gray).

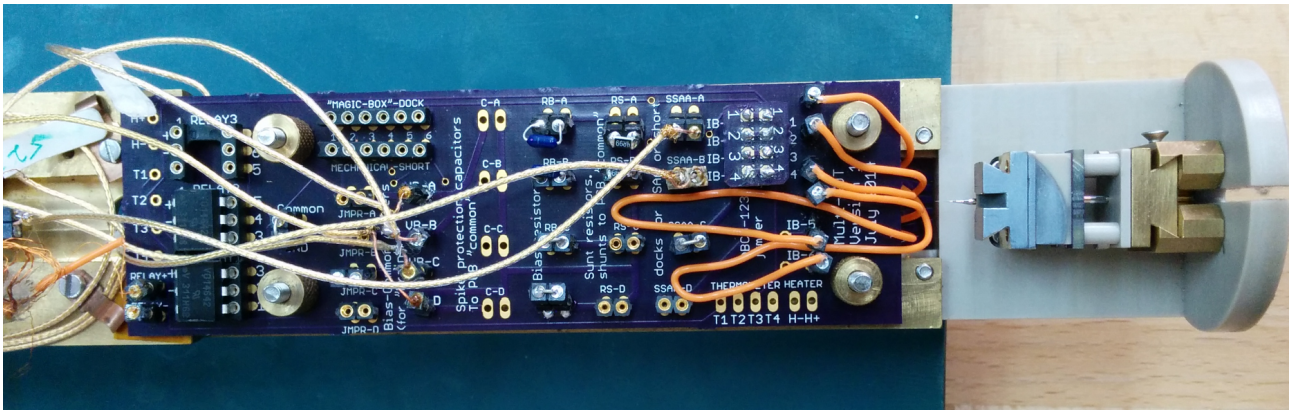

Figure 28: A photograph of the PCB in the configuration used for taking the data presented in this work.

8.4.2 White noise diode circuit

The white noise measurement circuit is presented in Figure 7c. The principle of operation is as follows. The voltage V_{FB} which is proportional to the current through the MSOT (either I_1 or I_2) has a DC component as well as noise. The noise spectrum is composed of $1/f$ and white noise which dominates above ~1 kHz. To measure the white noise we first filter out the DC, then amplify the signal to bias the diode above its threshold. We also use the filtering capabilities of the amplifier to keep only the ~10 kHz component. The HPF (High Pass Filter) removes any DC offset on the amplifier's output. The diode is thus biased with the ~10 kHz component of the MSOT's noise. On the diode's output the signal is rectified, resulting in a nonzero DC component proportional to the amplitude of the unrectified signal. The DC component is measured with a voltmeter. The calibration is done by simultaneously measuring the DC voltage V_{diode} on the white noise circuit's output and the spectrum directly on V_{FB} with a spectrum analyzer, taking an average value around 10 kHz, denoted S_V. We repeat the measurement for different biases therefore different noise levels to get statistics and eventually use a linear fit to get $S_V(V_{diode})$. An example of the calibration appears in Figure 30.

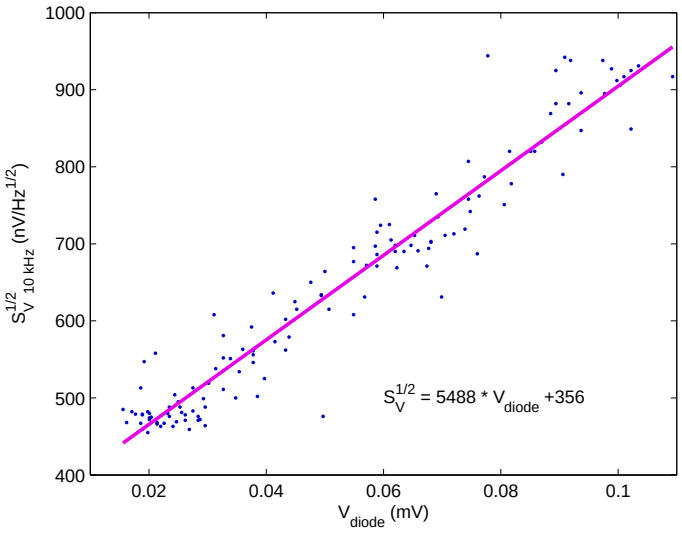

Figure 29: Diode circuit calibration. The calibration is done by simultaneously measuring the DC voltage on the diode's circuit and the 10 kHz white noise component of the V_{FB} spectrum taken with the spectrum analyzer. The linear fit coefficients are given in units of $\left(\mathrm{nV}/\sqrt{\mathrm{Hz}}\right)/\mathrm{mV}$ and $\mathrm{nV}/\sqrt{\mathrm{Hz}}$.

The full details of the circuit's components are given here, reviewing it from left to right. The BPF is composed of three filters in series:

1. A four stage HPF with a cutoff frequency of 1.5 kHz and roll-off of 80 dB/decade, composed of four 2.2 nF capacitors and four 48 kΩ shunt resistors,

2. A two stage HPF with a cutoff frequency of 10 kHz and roll-off of 40 dB/decade, composed of two 1 nF capacitors and two 15 kΩ shunt resistors and

3. A two stage Low Pass Filter (LPF) with a cutoff frequency of 300 kHz and roll-off of 40 dB/decade, made of two 0.5 kΩ resistors and two 1 nF shunt capacitors.

The first amplifier is a Stanford amplifier set to $G_1 = 2 \times 10^4$ set to high reserve, with both its LPF and HPF set to 10 kHz.

After the Stanford, the HPF is a two stage, 0.8 kHz cutoff frequency with a roll-off of 40 dB/decade which is made of two 100 nF capacitors and two 2 kΩ shunt resistors.

The diode is a high performance Herotek DZM040AA. It has a built in shunt $R_{sd} = 50\ \Omega$ inside its casing connected to its output. The resistor R_{sd} that appears in the circuit schematics was not added outside the diode - it is inside its casing. To verify this one can simply measure the diode's output impedance to find it is 50 Ω.

8.5 Additions to the theoretical analysis

8.5.1 I_c calculation

Step 1 - DC Kirchhoff calculation The purpose of the following calculation is to relate the circuits external parameters, namely V_{B1} and V_{B2} to the MSOT intrinsic quantities I_1 and I_2, in the SC state. It is also used as the first step in numerical calculation of the critical currents $I_{c,i}(B_a, V_{B2})$. The Kirchhoff equations for the circuit, applicable only in the *SC* state, are given in section 5.2.1. These are 5 linear equations and 7 unknowns. The passive resistances are taken as parameters. It allows solving for 5 of the 7 unknowns, as function of the remaining 2 unknowns. For example, one can choose to leave I_1 and V_{B1} as unknowns and solve for all other 5. The solution to one of the variables is:

$$I_2(V_{B1}, I_1) = -\left(\frac{R_{B1}}{R_{B1}+R_{S1}}\frac{R_{S1}+R_{P1}+R_{P3}}{R_{P3}} + \frac{R_{S1}}{R_{B1}+R_{S1}}\frac{R_{P1}+R_{P3}}{R_{P3}}\right) I_1 + \frac{R_{S1}}{R_{P3}(R_{B1}+R_{S1})} V_{B1}.$$

We can now approximate this using $R_{S1} \ll R_{B1}$, $\frac{R_{S1}}{R_{B1}}\frac{R_{P1}}{R_{P3}} \ll 1$, $I_{B1} \approx \frac{V_{B1}}{R_{B1}}$ to get equation 14. Since the circuit's branches 1 and 2 are symmetric, the results are also applicable with the indices replacement $1 \longleftrightarrow 2$.

Another interesting solution: Let us now calculate $I_1(I_{B1}, I_{B2})$:

$$I_1(I_{B1}, I_{B2}) = \frac{(R_{P2}R_{S1} + R_{P3}R_{S1} + R_{S1}R_{S2})I_{B1} - R_{P3}R_{S2}I_{B2}}{R_{P1}R_{P2} + R_{P1}R_{P3} + R_{P2}R_{P3} + R_{P1}R_{S2} + R_{P2}R_{S1} + R_{P3}R_{S1} + R_{P3}R_{S2} + R_{S1}R_{S2}}.$$

Assuming $R_{Si} = R_S$ and $R_{Pi} = R_P$ we get:

$$I_1(I_{B1}, I_{B2}) = \frac{\left(2R_PR_S + R_S^2\right)I_{B1} - R_PR_SI_{B2}}{3R_P^2 + 4R_PR_S + R_S^2}.$$

$I_2(I_{B1}, I_{B2})$ is found by replacing the indices $1 \longleftrightarrow 2$.

Step 2 - Lagrange multipliers In section 5.2.2 we treated the Lagrange multipliers method. The full equation we get when applying $\nabla_{\gamma_i}\mathscr{L} = 0$ and solving for $\gamma_1(\gamma_2, \gamma_3)|_{I_{c1}}$ is

$$\frac{K_2K_3K_4 + K_1K_3K_4 + K_1K_2K_4 + K_1K_2K_3 + K_1K_2K_3K_4\pi\beta_L}{K_3\left((R_{B1}R_{P1} + R_{B1}R_{S1} + R_{P1}R_{S1})4K_1 - (R_{B1}+R_{S1})4R_{P3}K_2 + (R_{B1}(R_{P1} - R_{P3} + R_{S1}) + R_{S1}(R_{P1} - R_{P3}))\pi\beta_LK_1K_2\right)} = 0,$$

where we denoted $K_i = a_i\cos\gamma_i$. By taking the numerator and dividing it by $K_1K_2K_3K_4$ we got the simplified version in equation 19 which is valid as long as the K_is and the denominator are all different than zero. For example, in the case $K_2 = a_2\cos\gamma_2 = 0$, corresponding to $J_2 = \sin\gamma_2 = \pm 1$, we get the equation $K_1K_3K_4 = 0$ which means that the critical current will occur when either K_1, K_3 or K_4

will be zero. For the denominator to be different from zero we must demand (approximating using $R_{B1} \gg R_{S1}$): $K_3 \neq 0$ and $\left(\frac{R_{P1}+R_{S1}}{R_{P3}} + \frac{R_{P1}-R_{P3}+R_{S1}}{4R_{P3}}\pi\beta_L K_2\right) K_1 \neq K_2$.

Step 3 - mapping to the circuit parameters Solving for $V_{B2}(I_1, I_2)$ gives:

$$V_{B2} = \left(1 + \frac{R_{B2}}{R_{S2}}\right) R_{P3} I_1 + \left(R_{B2}\left(1 + \frac{R_{P2}+R_{P3}}{R_{S2}}\right) + R_{P2} + R_{P3}\right) I_2,$$

which can be approximated, using $R_{Bi} \gg R_{Si}, \quad R_{Bi} \gg R_{Pi}$ to be:

$$\frac{V_{B2}}{R_{B2}} = \frac{R_{P3}}{R_{S2}} I_1 + \left(1 + \frac{R_{P2}+R_{P3}}{R_{S2}}\right) I_2,$$

as given in section 5.2.3.

8.6 Johnson noise in the SC state

The current Johnson noise for a resistance R is

$$\sqrt{S_i} = \sqrt{\frac{4k_B T \Delta f}{R}}.$$

The effective resistance of the current loop is

$$R_{1eff} = R_{P1} + R_{S1} + \left[R_{P3}^{-1} + (R_{P2} + R_{S2})^{-1}\right]^{-1} + R_{MSOT} \approx R_{P1} + R_{S1} + R_{P3} + R_{MSOT},$$

where R_{MSOT} is the MSOT's resistance which is between 0 Ω at the SC state to a few kΩ in the voltage state. In the last step we assumed $R_{P3}^{-1} \gg (R_{P2} + R_{S2})^{-1}$, which is true for the MSOT presented in this work for which $R_{pi} \approx 1\ \Omega$ and $R_{S1} = 5\ \Omega$. The Johnson noise on I_1 due to the circuit at 4.2 K is thus:

$$\sqrt{S_{i1}} \approx 5.7\ \text{pA}/\sqrt{\text{Hz}}.$$

The SSAA current noise is of order $\sqrt{S_{i,SSAA}} \approx 4\ \text{pA}/\sqrt{\text{Hz}}$ and adding them would be

$$\sqrt{S_{i,tot}} \approx \sqrt{S_{i,SSAA} + S_{i1}} = 7\ \text{pA}/\sqrt{\text{Hz}}.$$

We wish to compare this calculated Johnson noise with the actual measured white noise in the SC state. This noise was measured by the diode circuit. A more accurate measurement for the noise was done by the spectrum analyzer, but was only taken at the working points and not in the SC state. We recalibrate the diode noise measurement according to the spectrum analyzer measurement by comparing both data sets at the same working points. The recalibration is done by plotting both data sets one against the other and taking a linear fit $y = ax + b$, where x and y represents the spectrum

analyzer and diode data respectively and a and b are the linear fit's slope and intercept respectively (see Figure 30). After recalibration both data sets should give on average the same value. To test this we do another linear fit after the calibration and expect to get a zero intercept and a slope of 1. The recalibrated diode noise is then given by:

$$\sqrt{\tilde{N}_V} = \frac{\sqrt{N_V} - b}{a},$$

where the tilde denotes precalibrated data. The average noise measured by the diode in the SC state before recalibration is $\sqrt{\tilde{N}_V}|_{SC} = 500 \pm 150\, n\mathrm{V}/\sqrt{\mathrm{Hz}}$, the error representing one standard deviation. After recalibration it reads $\sqrt{N_V}\,(30\,\mathrm{kHz})\,|_{SC} \approx 365 \pm 105\ \mathrm{nV}/\sqrt{\mathrm{Hz}}$, which corresponds to a current noise of

$$\sqrt{S_{i,SC}} \approx 14 \pm 4\ \mathrm{pA}/\sqrt{\mathrm{Hz}},$$

which is a factor 2 more than the theoretical calculation presented above.

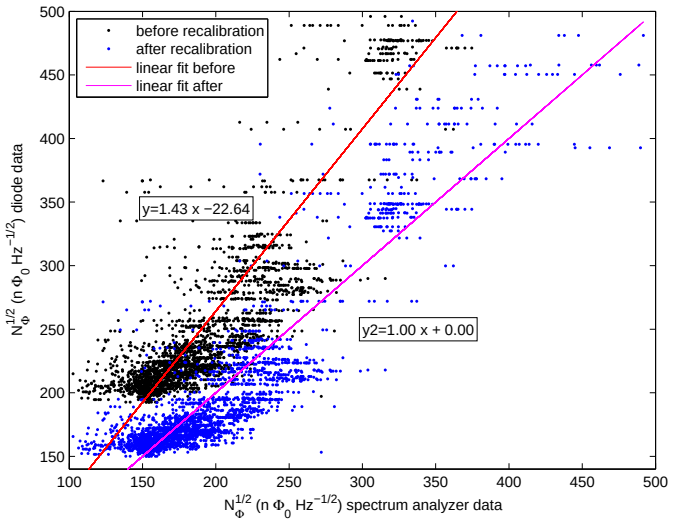

Figure 30: Recalibration of the flux noise measured by the diode at 10 kHz according to the flux noise measured by the spectrum analyzer at 30 kHz.